

Variable Point Sources in Sloan Digital Sky Survey Stripe 82.

I. Project Description and Initial Catalog ($0 \text{ h} \leq \alpha \leq 4 \text{ h}$)

Waqas A. Bhatti¹, Michael W. Richmond², Holland C. Ford¹, Larry D. Petro³

ABSTRACT

We report the first results of a study of variable point sources identified using multi-color time-series photometry from Sloan Digital Sky Survey (SDSS) Stripe 82, including data from the SDSS-II Supernova Survey, over a span of nearly ten years (1998–2007). We construct a light-curve catalog of 221,842 point sources in the RA 0 to 4 h half of Stripe 82, limited to $r = 22.0$ mag, that have at least 10 detections in the *ugriz* bands and color errors < 0.2 mag. These sources are then classified by color and by cross-matching them to existing SDSS catalogs of interesting objects. Inhomogenous ensemble differential photometry techniques are used to greatly improve our sensitivity to variability and reduce contamination by sources that appear variable due to large photometric noise or systematic effects caused by non-uniform photometric conditions throughout the survey. We use robust variable identification methods to extract 6,520 variable candidates from this dataset, resulting in an overall variable fraction of $\sim 2.9\%$ at the level of ~ 0.05 mag variability. Despite the sparse and uneven time-sampling of the light-curve data, we discover 143 periodic variables in total. Due to period ambiguity caused by relatively poor phase coverage, we identify a smaller final set of 101 periodic variables with well-determined periods and light-curves. Among these are 55 RR Lyrae, 30 eclipsing binary candidates, and 16 high amplitude Delta Scuti variables. In addition to these objects, we also identify a sample of 2,704 variable quasars matched to the SDSS Quasar Catalog (Schneider et al. 2007), which make up a large fraction of our variable candidates. An additional 2,403 quasar candidates are tentatively identified and selected by their non-stellar colors and variability. A sample of 11,328 point sources that appear to be non-variable given the limits of our variability sensitivity is also briefly discussed. Finally, we describe several interesting objects discovered among our eclipsing

¹Department of Physics & Astronomy, Johns Hopkins University, 3400 N. Charles St., Baltimore, MD 21218, email: waqas@pha.jhu.edu

²Department of Physics, Rochester Institute of Technology, 84 Lomb Memorial Dr., Rochester, NY 14623

³Space Telescope Science Institute, 3700 San Martin Dr., Baltimore, MD 21218

binary candidates, and illustrate the use of our publicly available light-curve catalog¹ by tracing Galaxy halo substructure with our small sample of RR Lyrae variables.

Subject headings: binaries: eclipsing — catalogs — stars: variables: other — surveys

1. Introduction

The last fifteen years have yielded a wealth of new knowledge of many types of astronomical objects due to the prevalence of large scale surveys such as the Sloan Digital Sky Survey (SDSS; York et al. 2000) and the Two-Micron All Sky Survey (2MASS; Skrutskie et al. 2006). These surveys cover large areas of the sky, are deep, are sensitive to many different types of objects, and most importantly, have uniform data reduction and characterization. Powerful data access tools made available to the community allow efficient dissemination and data-mining, and allow large populations of objects to be studied all at once.

The next generation of astronomical surveys will include a powerful new tool: the exploration of the time-domain. Many classes of astronomical objects vary over differing timescales, so a uniform approach that covers all of these timescales while covering large portions of the sky will produce a diverse catalog of variable objects that may be studied in much the same manner as the static sky has been studied using SDSS and 2MASS. Two such projects in advanced stages of planning and development are the Pan-STARRS project (Kaiser et al. 2002; currently undergoing commissioning) and the Large Synoptic Survey Telescope (LSST; Tyson 2002; Ivezić et al. 2008; expected to start observations in 2015).

On a smaller scale, the variable sky has been explored by many successful projects, including OGLE (towards the Galactic Bulge; Udalski et al. 2002), MACHO (Galactic Bulge and Magellanic Clouds; Alcock et al. 2001), and ASAS (all-sky to $V = 15.0$; Pojmanski 2002). Photometric surveys for transiting planets in recent years, such as HAT (Bakos et al. 2002), TrES (Alonso et al. 2004), SuperWASP (Pollacco et al. 2006), and XO (McCullough et al. 2006) have also resulted in studies of several classes of variable stars. In addition to these surveys, specialized searches for supernovae, including the CFHT Supernova Legacy Survey (Sullivan et al. 2005) and the SDSS-II Supernova Survey (Frieman et al. 2008), can provide large and uniform datasets suitable for the identification and characterization of many different types of variable sources.

¹Available at <http://shrike.pha.jhu.edu/stripe82-variables>

Although the SDSS is largely a single-epoch survey, it covers some regions of the sky multiple times. The most prominent of these is a region on the celestial equator known as Stripe 82. This region has been surveyed repeatedly by the SDSS over many years, most recently by the SDSS-II Supernova Survey, and has been studied for variability by several authors. Sesar et al. (2007) presented a catalog of 13,051 variable star candidates discovered using observations of the Stripe carried out before the advent of the SDSS-II Supernova Survey. Bramich et al. (2008) published a light-curve catalog of Stripe 82, incorporating data from the first two years of the Supernova Survey. Blake et al. (2008) discovered a low-mass eclipsing binary in this region, using light-curves also generated from the first two years of the Supernova Survey. Becker et al. (2008) reported another low mass eclipsing binary discovered in the footprint of Stripe 82, but using calibration data from 2MASS. More recently, Watkins et al. (2009) and Kowalski et al. (2009) have presented catalogs of RR Lyrae and M-dwarf flare stars present in Stripe 82 respectively.

Here, we construct a light-curve catalog for a magnitude limited sample of point sources in SDSS Stripe 82, using data ranging from the first observations of this area of sky in 1998 to the high cadence observations carried out by the SDSS-II Supernova Survey (2005–2007). We use inhomogeneous ensemble differential photometry to remove systematic artifacts from these light-curves caused by variable photometric conditions. Point sources are then classified by color and by cross-matching to other catalogs of interesting objects in Stripe 82. The large number of observation epochs available in our dataset then allows robust identification of variable sources, especially periodic variables.

We first construct a light-curve catalog of variable point sources detected in Stripe 82. We then concentrate on three classes of periodic variables: eclipsing binaries, RR Lyrae, and Delta Scuti, and present periods and phase-folded light-curves for all such objects identified. In addition, we use the color and variability properties of quasi-stellar objects (QSOs) matched to the SDSS Quasar Catalog (Schneider et al. 2007) to identify a new sample of variable candidate QSOs in our light-curve catalog. Finally, we extend the work of Ivezić et al. (2007) by using a larger number of observation epochs and our robust variable extraction methods to identify a sample of objects that appear *nonvariable* at the limits of our sensitivity.

In this paper (the first of two), we first describe how we extract objects from the detection catalogs from the SDSS pipeline, and subsequently organize and generate an initial light-curve catalog for the RA 0 to 4 h half of Stripe 82 (Section 2). We describe the inhomogeneous ensemble differential photometry algorithms in detail (Section 2.3), and then discuss how point source classification and variable extraction are implemented (Sections 2.4 and 3.1). Two independent period search algorithms are described and the difficulties

we face in searching for periodic variability in our sparse and unevenly sampled dataset are also outlined (Section 3.2). We then apply these variable extraction and period finding algorithms to objects in the RA 0 to 4 h half of Stripe 82, and describe the general properties of variables discovered after processing this initial light-curve catalog (Section 4.1).

We characterize the completeness and efficiency of our variable extraction pipeline by carrying out end-to-end simulations of the entire process (Section 4.2). Our period finding algorithms are analyzed in a similar manner and provide estimates for the efficiency and completeness of our periodic variable sample. Instructions on how to access our publicly available data are then provided (Section 4.3). We then present and discuss the properties of eclipsing binaries, RR Lyrae, and Delta Scuti variables identified in this initial light-curve catalog (Section 4.4). Finally, we discuss samples of candidate QSOs and nonvariable objects also identified by our pipeline (Sections 4.5 and 4.6). The second paper in this series will complete our light-curve catalog by adding objects and variables identified in the RA 20 to 0 h half of Stripe 82, and extend the discussion of their properties in the context of a completely processed sample.

2. Data from SDSS Stripe 82

2.1. Overview

The Sloan Digital Sky Survey (SDSS) uses a dedicated 2.5-m telescope located at the Apache Point Observatory in New Mexico. During imaging, the telescope points at a fixed declination on the meridian and scans the sky using the time-delay and integrate mode that clocks the charge across the charge-coupled device arrays (CCDs) at the sidereal rate. The record of one particular scan of a $\sim 1.3^\circ$ -wide *strip* is called a *run*. Two overlapping *strips* make up one *stripe*; as a result, each *stripe* is $\sim 2.5^\circ$ wide. Each run exposes five CCDs in five filters, *u*, *g*, *r*, *i*, and *z* for approximately 54 seconds per pixel. One run is further broken up into *fields*, which are $13' \times 10'$ each. Detections are fed through the SDSS photometric pipeline, are classified by morphological type, and are assigned magnitudes and associated uncertainties. Point source objects are well described by fitting a point spread function to the detection, resulting in so-called PSF magnitudes, while extended source objects are characterized by model magnitudes. Details of the SDSS photometry and classification algorithms may be found in Gunn et al. (2006), Lupton et al. (2002), Stoughton et al. (2002), Hogg et al. (2001), and references therein. Observations take place on nights that have seeing better than $1.7''$ (FWHM), are moonless, and show little transparency variation due to cloud cover (York et al. 2000; Hogg et al. 2001).

Stripe 82 is on the celestial equator, ranging from 20 h to 4 h in right ascension and -1.27° to $+1.27^\circ$ in declination, for a total area of about 300 sq. deg. The region is at high Galactic latitude, ranging from -30° to -70° in Galactic latitude and between 40° and 200° in Galactic longitude. The Stripe has been observed many times over the 10 years of operation of SDSS and SDSS-II, mostly during the fall (September – December). Figure 1 (left panel) shows the temporal coverage of the Stripe as a function of time over all ten years of observation.

Starting with commissioning runs in 2004, and full operations in 2005, Stripe 82 was observed at higher cadence by the SDSS-II Supernova Survey (hereafter, the SN Survey; Frieman et al. 2008). The nominal time between consecutive observations of a field was roughly 2 days (see Figure 1, right panel). The SN Survey was designed to obtain a uniform sample of medium-redshift ($z \sim 0.05 - 0.35$) Type Ia supernovae for the purposes of precision cosmology. The requirement for improved temporal coverage necessitated a compromise on the photometric quality. As a result, the SN Survey observed on nights that would not have been designated as photometric for the legacy SDSS. This relaxed photometric quality requirement poses a challenge for identification of ‘true’ variables from the dataset, as we will note in Section 2.3.

In our dataset, we have 242 runs from Stripe 82: 69 from observations of the Stripe before the SN Survey, 65 for the first season of the SN Survey in 2005, 86 runs during the second season in 2006, and 22 runs during the final season in 2007². We obtained the pre-SN Survey data for Stripe 82 using the Catalog Archive Server (CAS) SQL interface³ to the SDSS database, downloading FITS files with lists of object detections per run along with their photometric properties. The data for the SN Survey was reduced by the SDSS photometric pipeline and made available on the SDSS Data Archive Server⁴ as calibrated object catalogs (tsObj FITS binary table files, one per field) and calibrated images (fpC FITS image files, one per field). We downloaded the calibrated object catalogs in form of tsObj FITS files for runs associated with the SN Survey, put them together with the object catalogs for the pre-SN Survey runs obtained earlier, and then processed all 242 runs through a multi-stage pipeline designed to extract suitable point sources and search for possible variables. An overview of the pipeline is given in Figure 2, while details are discussed below.

²A full list of runs used is available at our catalog’s website.

³<http://casjobs.sdss.org/CasJobs/>

⁴See <http://das.sdss.org/www/html/imaging/dr-byRun-74.html>.

2.2. Object Extraction and Pre-Ensemble Processing

The data fields extracted from the SN Survey data are listed in Table 1. We imposed a uniform set of quality conditions using status and quality flags available in the tsObj and CAS output FITS files⁵. We first required that a detected object: (1) was not marked as saturated (BRIGHT and SATURATED flags set to 0), (2) was not a deblended child of a nearby object (PARENT set to -1, or PARENTID set to 0), (3) had no deblended children itself (NCHILD set to 0), (4) had the EDGE flag set to 0. Second, we required a detected object’s STATUS flags included SET, GOOD, OK_RUN, OK_SCANLINE, OK_STRIPE all set to 1, in addition to either PRIMARY or SECONDARY set to 1. We explicitly discarded all objects that had a status flag of DUPLICATE set to 1, indicating a duplicate detection within the same observation run (in overlapping adjacent fields for example). Third, we ensured that an object had valid magnitudes recorded in all five bands by requiring that these measured values all be greater than -9999.0. Finally, we imposed a faint PSF magnitude limit of $z = 21.0$. Although we extracted both PSF and fiber magnitudes for each object from the catalogs, we only used the PSF magnitudes for all of our subsequent processing and variability analysis.

We then extracted only those objects classified by the SDSS photometric pipeline as point sources, by requiring the object TYPE flag be set to 6 (STAR). This left us with 57,406,616 point source detections over all runs. We then constructed a canonical match template for the entire Stripe using object detections in four high photometric quality SN Survey runs: North runs 5610 (MJD 53628) and 6430 (MJD 54011), and South runs 5776 (MJD 53669) and 6425 (MJD 54010). These runs were chosen because of acceptable seeing on these nights (median of $1.7''$) and full coverage of the Stripe from 20 h to 4 h in right ascension. Detections were matched between these runs using a $5.0''$ radius, and multiple detections of the same object discarded. The final match template then contained all point sources detected at least once in any of these runs, for a total of 2,000,242 objects.

We then matched all detections over all runs to the match template using a $5.0''$ match radius. All detections grouped inside this match radius were considered detections of a single match template object, and constituted a *match bundle*. The typical separation between neighboring point sources in our match template is $\sim 35''$. This is comfortably larger than our chosen match radius, so there is little chance of a detection being mistakenly associated with a nearby match template object. We also note that the match radius sets a rough upper limit of $\sim 0.5'' \text{ yr}^{-1}$ for the proper motion of any one match template object, assuming it is detected over all 10 years of temporal coverage.

⁵See <http://www.sdss.org/dr7/products/catalogs/flags.html> for details.

Figure 3 presents the distribution of the number of detections per match bundle. There are 473,759 objects (23.7% of the total) that have fewer than 10 detections in all 242 epochs over all 10 years of available photometric data. Of these, $\sim 28.6\%$ have only a single detection, $\sim 35.4\%$ have extreme colors⁶ most likely due to unreliable photometry, and $\sim 55.8\%$ are faint⁷. In contrast, only $\sim 0.2\%$ of objects with at least 10 detections have extreme colors, while only $\sim 2.3\%$ of the objects with at least 10 detections are classified as faint. We, therefore, err on the side of caution and remove all objects with fewer than ten detections from any further consideration to keep contamination by unreliable photometry to a minimum. As a result, we have 1,526,483 objects with 55,610,252 total detections in our final point source light-curve catalog for Stripe 82. We carry this catalog forward to the ensemble photometry stage of our processing pipeline, described below.

2.3. Ensemble Differential Photometry

As discussed earlier, the SN survey sacrifices some photometric quality to gain temporal coverage. Unfortunately, this means that observations are taken under all kinds of photometric conditions, including sub-optimal seeing, variable transparency, and at all lunar phases except for full moon. We note that the Stripe 82 runs before the SN Survey have more stringent constraints on these variables, and are generally of higher photometric quality. Even these observations, however, suffer from variable photometric conditions on time-scales of minutes to hours (see Ivezić et al. 2007 for details). We, therefore, face the challenge of reconciling the low cadence but relatively high quality measurements taken before the SN survey with measurements of lower quality at much higher cadence taken during the Survey.

In particular, identification of variable objects becomes problematic when large systematic effects caused by night-to-night sky and seeing variations are present. This is illustrated by an example relation between median SDSS light-curve magnitude and light-curve standard deviation (Fig 4, top-left and top-right panels). This relation is often used to identify obvious variable objects; these lie above the general trend. It is difficult to identify true variables, however, when the relation itself has a scatter caused by magnitude measurements affected by differing photometric conditions. In addition, as seen in the left panel of Figure 5, these systematic effects usually appear as dips in light-curves on specific observation dates. These dips can be very large and affect measurements in all bands for all objects in a field,

⁶Defined as $|u - g| > 3.0$ or $|g - r| > 3.0$ or $|r - i| > 3.0$ or $|i - z| > 3.0$.

⁷Defined as g and $r > 22.2$, $i > 21.3$. These are the 95% point source detection repeatability limits for these bands. See <http://www.sdss.org/dr7> for details.

thus artificially increasing the light-curve standard deviation of even completely nonvariable objects.

Such artifacts are usually removed in variability studies by the use of differential photometry. A target star is compared to an ensemble of comparison stars, and the measured magnitudes normalized to a weighted ensemble magnitude. The resulting differential magnitude for the target object removes any systematic variation in photometric conditions that affects all stars being observed on the same night. This technique is powerful and has been widely deployed, owing to its computational simplicity, as well as the very high photometric precisions that are possible. We, however, cannot employ this simple differential photometry method, because we are not guaranteed to have the same comparison stars in the ensemble for any one target star over all observations. Furthermore, we must ensure that all comparison stars are not intrinsic variables themselves; this is not possible *a priori* when studying light-curves of ~ 1.5 million objects. We turn, therefore, to a differential photometry technique known as inhomogeneous ensemble photometry (Honeycutt 1992). The general method is described immediately below; a discussion of its application to our dataset follows thereafter.

We first assume that most of the stars in a given field containing a target star are nonvariable, and that the measured magnitude of any one star i at a time index value of j is given by

$$m(i, j) = m_0(i) + e(j), \quad (1)$$

where $m(i, j)$ is the measured magnitude of a star, $m_0(i)$ is the ‘true’ mean magnitude that would have been measured in the absence of photometric condition variations, and $e(j)$ represents the change in photometric zero-point caused at time index j by these variations and is applied to all stars in the field at that time index. We must minimize the quantity β , given by

$$\beta = \sum_{i=1}^{N_{stars}} \sum_{j=1}^{N_{obs}} [m(i, j) - m_0(i) - e(j)]^2 w(i, j), \quad (2)$$

where $w(i, j)$ is the weight associated with a measured magnitude $m(i, j)$ and is given by

$$w(i, j) = w_1(j)w_2(i)w_3(i, j)w_4(i, j). \quad (3)$$

The weights w_1 , w_2 , and w_3 are either zero or one, while w_4 is the statistical weight based on the uncertainty of measurement $\sigma[m(i, j)]$ for $m(i, j)$ and is calculated as $1/\sigma^2[m(i, j)]$. The weight $w_1 = 0$ if the observation at time index j is to be excluded, $w_2 = 0$ if the star i is to be excluded, and $w_3 = 0$ if a specific observation of star i at time index j is to be excluded from the photometric solution. Once this solution is computed, and we have obtained the ‘true’ mean magnitudes $m_0(i)$ of all stars in the ensemble, along with the error terms $e(j)$,

we can solve for the corrected magnitude $M(i, j)$ for any star i at time index j :

$$M(i, j) = m(i, j) - e(j). \quad (4)$$

Finally, we can calculate the variance of the ‘true’ mean magnitudes $\sigma^2[m_0(i)]$ using:

$$\sigma^2[m_0(i)] = \frac{N_{obs} \sum_{j=1}^{N_{obs}} [M(i, j) - m_0(i)]^2 w(i, j)}{(N_{obs} - 1) \sum_{j=1}^{N_{obs}} w(i, j)}. \quad (5)$$

The relation between $m_0(i)$ and $\sigma[m_0(i)]$ is equivalent to the usual magnitude- σ relation. Objects with large values of $\sigma[m_0(i)]$ relative to the general trend at that magnitude may be considered as possible variables.

In practice, our inhomogeneous ensemble photometry implementation⁸ normalizes the ‘true’ mean magnitude $m_0(i)$ for a star i to the ‘true’ mean magnitude of the brightest star in the ensemble, resulting in effective differential magnitudes $M(i, j)$ for all of the stars. We use the weights w_1 , w_2 , and w_3 to take into account the presence or absence of comparison stars in the ensemble from night to night. To deal with the problem of comparison stars being possible variables, we run the photometric solution for a target three times, each time removing all comparison stars from the ensemble that appear to be variable. The ensemble itself is chosen such that it has at least 10 comparison stars observed within 10 seconds of the time of observation of the target star (so within 150 arcseconds of the position of the target star, assuming tracking at sidereal rate). The median number of comparison stars is ~ 80 per target star. This set of conditions ensures that we obtain the best possible differential magnitude for the target on each night that it is observed. At this stage, we also remove from any further consideration all target stars that do not have comparison star ensembles satisfying these conditions, since reliable differential photometry is not possible for these objects. In the processing of our RA 0 to 4 h light-curve catalog, this removes only 2,653 objects ($\sim 0.72\%$ of the total) from consideration.

We show the impact of inhomogeneous ensemble photometry in Figures 4 and 5. The relation between the median light-curve magnitude and the differential light-curve standard deviation (Fig 4, bottom-left and bottom-right panel) is seen to be much improved, with much of the extrinsic scatter removed. Furthermore, the light-curves of the target object and its four closest neighbors (Fig 5, right panel) no longer suffer from the systematic effects seen in the left panel.

The fourth order polynomial fits to the empirical relation between the mean SDSS light-curve magnitude (in each band $ugriz$) and the differential magnitude light-curve standard

⁸See M. W. Richmond’s website: <http://spiff.rit.edu/ensemble>.

deviation σ calculated using differential magnitude light-curve data for 365,086 objects with at least 10 observations from our initial light-curve catalog (RA 0 to 4 h) are given below:

$$\sigma(u) = 105.94 - 24.197u + 2.0621u^2 - 0.07772u^3 + 0.00109u^4, \quad (6)$$

$$\sigma(g) = 51.441 - 11.337g + 0.93529g^2 - 0.03423g^3 + 0.00047g^4, \quad (7)$$

$$\sigma(r) = 48.684 - 10.831r + 0.90210r^2 - 0.03334r^3 + 0.00046r^4, \quad (8)$$

$$\sigma(i) = 54.844 - 12.291i + 1.0315i^2 - 0.03842i^3 + 0.00054i^4, \quad (9)$$

$$\sigma(z) = -69.446 + 15.591z - 1.0329z^2 + 0.04799z^3 - 0.00066z^4. \quad (10)$$

We generate differential magnitude light-curves in all five bands for all objects in our light-curve catalog and search them for variability. The large number of stars in our dataset, coupled with the numerous lookups required to build each target star’s comparison ensemble, make this stage in our pipeline the most computationally intensive, and thus, the slowest.

2.4. Classification of Point Sources

We classify the point sources in our final light-curve catalog in two ways. First, we cross-match objects between our catalog and existing catalogs of interesting and possibly variable objects in the SDSS, especially those present in the Stripe 82 footprint. Second, we use several selection algorithms to sort objects into rough classification bins by their SDSS colors. In this way, we can select interesting populations of objects to study for variability without having to resort to spectra.

Several authors have already compiled catalogs of interesting classes of point source objects discovered during SDSS operations. Schneider et al. (2007) reported the discovery of 77,429 quasars ranging in redshift from 0.08 to 5.41, covering 5,740 sq. deg of sky. Most quasars are suspected to be variable in some degree; our catalog of multi-color light-curves covering a base-line of nearly ten years may be used to test that assumption. Other catalogs that include possible variable objects include a catalog of 9,316 spectroscopically confirmed white-dwarfs and 948 hot sub-dwarfs by Eisenstein et al. (2006), and the already mentioned SDSS Stripe 82 catalog of variable stars by Sesar et al. (2007), containing 13,051 sources (hereafter referred to as the SDSS-I Variable Object Catalog). We also cross-match our catalog with the Stripe 82 Standard Star Catalog (containing ~ 1 million objects) generated by Ivezić et al. (2007), to confirm the nonvariability of these objects and their suitability for use as faint standard stars. We use a $5.0''$ radius to match between all of the preceding catalogs and our catalog of match template objects.

In addition to classifying objects in this way, we also make use of the excellent color

selection made possible by the five photometric bands used in the SDSS. Specifically, we use the median SDSS light-curve colors $u - g$, $g - r$, $r - i$, and $i - z$ for each object. We use color selection algorithms from three sources: (1) spectroscopic target selection color cuts from the SDSS-II Sloan Extension for Galactic Understanding and Exploration (SEGUE; Yanny et al. 2009) to select different types of stellar objects, (2) colors from Sesar et al. (2007) to identify potential RR Lyrae, and (3) color cuts for M-dwarfs in West et al. (2008). Table 2 presents the color classification schemes we use for our catalog. The SDSS photometric pipeline reports magnitudes measured for each detection, and the extinction in magnitudes at the position of the detection. We use these measurements and calculate the dereddened magnitudes for all objects. These are then used for all color selection cuts, except where noted in Table 2. We do not use dereddened colors for brown dwarfs and main-sequence/white-dwarf pair selection because these faint objects are likely to be nearby. We note that any one point source may be assigned multiple categories based on color; these are all noted in *classification tags* associated with that point source in our catalog. Objects that are not matched to any of the catalogs listed above and cannot be classified using color are also noted and assigned a classification tag of *unknown*.

Results from the catalog cross-matching and color classification schemes above for the first release of our catalog are reported in Section 4. We now turn to the identification of variable objects in our catalog.

3. Variable Objects in Stripe 82

3.1. Extraction of Variable Point Sources

We identify possible variable sources in two steps. The first involves using the results from the ensemble photometry stage of our pipeline, specifically the relation between the differential magnitude light-curve standard deviation $\sigma[m_0(i)]$ (Equation 5) and the ‘true’ mean differential light-curve magnitude $m_0(i)$. As the ensemble differential photometry stage of our pipeline iterates over each target object, it generates a plot of this relation for all objects in its associated ensemble, and fits a second-degree polynomial to the empirical trend. Outliers more than $2\text{-}\sigma$ away from the general trend are iteratively discarded to make the fit more robust.

This procedure is then repeated to obtain such plots and trends for the u , g , r , i , and z bands separately. Examples of these plots are shown in Figure 6. These are then used to tag the target object as a *tentative variable* if: it lies at least $2\text{-}\sigma$ above the general trend of the magnitude-standard deviation relation in (1) u and g bands simultaneously, or (2)

g and r bands simultaneously, or (3) r and i bands simultaneously, or (4) i and z bands simultaneously. We also tag objects as tentative variables if they lie at least $1\text{-}\sigma$ above the general trend in all three of the r , i , and z bands simultaneously; this has the potential of picking up faint red variables in populations of K and M-dwarfs. This system, however, is not robust against false variability caused by large photometric noise for faint objects. These objects are likely to lie above the variability threshold due to their small numbers and large uncertainties, even in their differential magnitudes, and thus end up being erroneously tagged as tentative variables.

The second step involved in identifying variable sources corrects for this type of false variability. We employ the Stetson variability index (Stetson 1996). This is a measure of the correlation of simultaneous variability across a pair of bands. The Stetson variability index $J_{\alpha\beta}$ for two bands α and β observed at the same time is

$$J_{\alpha\beta} = \frac{\sum_{k=1}^n w_k \operatorname{sgn}(P_k^{\alpha\beta}) \sqrt{|P_k^{\alpha\beta}|}}{\sum_{k=1}^n w_k}, \quad (11)$$

where w_k is the weight assigned to k th pair of observations. The product of the normalized magnitude residuals P_k for the k th pair of observations is given by

$$P_k^{\alpha\beta} = \sqrt{\frac{n_\alpha}{n_\alpha - 1}} \sqrt{\frac{n_\beta}{n_\beta - 1}} \left(\frac{\alpha_k - \bar{\alpha}}{\sigma_{\alpha,k}} \right) \left(\frac{\beta_k - \bar{\beta}}{\sigma_{\beta,k}} \right). \quad (12)$$

where α_k and β_k are the magnitudes measured at time index k , $\sigma_{\alpha,k}$ and $\sigma_{\beta,k}$ are the errors associated with these measurements, $\bar{\alpha}$ and $\bar{\beta}$ are the weighted mean magnitudes, iterated as in Stetson (1996) to avoid outliers, and n is the number of observations. The Stetson variability index is large when the normalized magnitude residuals $P_k^{\alpha\beta}$ are correlated, as in the case of real variable sources. A nonvariable source, even one with a large light-curve standard deviation, will have uncorrelated magnitude measurements across pairs of bands. This will drive the Stetson index for such objects toward zero.

We calculate the Stetson variability indices J_{ug} , J_{gr} , J_{ri} , and J_{iz} using the differential *ugriz* magnitude light-curves obtained from the ensemble photometry procedure described in Section 2.3. Taking into account the variability index values for obvious variables in the dataset identified by inspection of a large number of differential magnitude light-curves (and phased differential magnitude light-curves in the case of periodic variables), we set a threshold index value of 0.3 to separate variable and nonvariable objects. Sources are therefore tagged as *probable variables* if: (1) any one of J_{ug} , J_{gr} , J_{ri} , and J_{iz} is greater than this threshold value, and (2) J_{gr} and J_{ri} are both greater than 0.0. Figure 7 shows the distributions of the calculated Stetson indices with their standard deviations (dot-dashed

lines) and threshold Stetson index value (dashed line) marked. Variable objects are selected relatively efficiently using our threshold Stetson index value.

Figure 8 shows the distribution of Stetson J_{gr} with median light-curve r magnitude for all 365,086 objects with at least 10 observations in the RA 0 to 4 h light-curve catalog. The underlying distribution shows no discernable trend with magnitude, indicating that the ensemble photometry routines combined with the Stetson index as an indicator of variability are quite robust in variable selection. Furthermore, as we go to fainter magnitudes (beyond $r \sim 22.0$), the distribution of the Stetson index no longer shows an outlying population of variables, indicating that these fainter objects have no correlated variability detected and thus appropriately have smaller Stetson index values. This points out the effective faint magnitude limit of our search for variability (discussed further in Section 4.1 below). We quantify the efficiency and robustness of our variable detection routines in Section 4.2 using synthetic light-curve catalogs and associated simulations of variability analysis.

Probable variables selected by this two part procedure can then be searched for periodic variability. If such variability exists, we generate estimates of the period, as described in Section 3.2 below.

3.2. Finding Periods

We search for periodicity among all objects marked as probable variables using two independent period-finding methods: the string length method of Dworetsky (1983), and a variation on the classic Lafler-Kinman phase-dispersion minimization algorithm (Lafler & Kinman 1965) used by Stetson (1996). Both of these methods attempt to minimize the sum of the dispersions of measurements ordered by phase for a test period (the ‘string length’), in order to produce the ‘smoothest’ possible light-curve. Perhaps their most important feature is that they do not involve the calculation of sinusoidal components for a light-curve, as in the Lomb-Scargle periodogram (Scargle 1982), and thus do not pre-suppose such a shape when searching for periods. This makes them invaluable for studying a broad range of periodic variable types, as expected in our dataset. These two algorithms also do not involve binning consecutive light-curve measurements, as seen in more sophisticated period finding methods such as AoV (Schwarzenberg-Czerny 1989), and BLS (Kovács et al. 2002). BLS and AoV do not work well on datasets such as ours, which have light-curves with a very small number of unevenly distributed and sparse time-series measurements over a long baseline.

The Dworetsky string length L_{dw} calculated for a test period and a series of phase-

ordered photometric measurements m_1 to m_N is given by the relation

$$L_{dw} = \sum_{i=1}^{N-1} \sqrt{(m'_{i+1} - m'_i)^2 + (\phi_{i+1} - \phi_i)^2} + \sqrt{(m'_1 - m'_N)^2 + (\phi_1 - \phi_N + 1)^2}, \quad (13)$$

where ϕ_i is the phase of observation i , and m' are modified magnitudes used to assign similar weights to the time and magnitude measurements, and are given by the relation

$$m'_i = (m_i - m_{min}) / (2.0(m_{max} - m_{min})) - 0.25, \quad (14)$$

where m_{min} and m_{max} are the minimum and maximum magnitude measurements in the timeseries, respectively.

The Stetson algorithm incorporates the weighting of individual light-curve measurements by their respective errors, thus, providing a more robust means of calculation of the string length. The Stetson string length L_{st} calculated for a test period and a series of phase-ordered photometric measurements m_1 to m_N is given by the relation

$$L_{st} = \frac{\sum_{i=1}^N w(i, i+1) |m_i - m_{i+1}|}{\sum_{i=1}^N w(i, i+1)}, \quad (15)$$

where w are the weights assigned to magnitudes m , which in turn have measurement errors σ . The expression $w(i, i+1)$ is given by the relation

$$w(i, i+1) = \frac{1}{[\sigma_i^2 + \sigma_{i+1}^2] [(\sigma_{i+1} - \sigma_i) + 1/N]}, \quad (16)$$

where σ_i is the measurement error associated with magnitude measurement m_i .

We calculate L_{dw} and L_{st} using *griz* differential magnitude light-curves for all objects tagged as *probable variables* using a test period interval of 0.1 to 100.0 days (see Figure 9 for an example) and a frequency step-size of 0.0001 days^{-1} . The *u*-band differential magnitude light-curves have poor signal-to-noise for many of the objects in our dataset, and are therefore not used for string length calculations. Objects with light-curve variations on longer time-scales (i.e. years) do exist in our dataset, but we do not attempt to fit periods to these, mainly due to extremely poor phase coverage (typically 40–60 unevenly sampled measurements over 10 years). If, upon inspection of its phased light-curve, an object appears to be variable on a time-scale shorter than 0.1 day, we rerun the period finding routines using a test period interval of 0.01 to 10.0 days.

For each object, we retain the test periods that result in the 20 shortest string lengths for both L_{dw} and L_{st} independently, and then phase-fold the light-curves using these periods.

The most likely period in each case is the one with the shortest string length. We require that the two period finding methods agree on the most likely period before accepting an object as a likely periodic variable. Further, we make use of the available multi-band photometric data by requiring that the most likely period reported by the string length algorithms be the same for each of the *gri* light-curves in the case of non-M dwarf objects, and for each of the *riz* light-curves for redder objects such as M-dwarfs. We then attempt to refine the period by rerunning the string length algorithms in a small period interval (typically 0.1 day) centered around the already determined most likely period. Finally, we visually inspect each phased light-curve obtained using this refined most likely period to assess its credibility, and place the object into one of three classification bins based on its light-curve shape: (1) eclipsing or ellipsoidal binary, (2) sinusoidal variable with an asymmetric light-curve, (3) and sinusoidal variable with a symmetric light-curve.

As mentioned earlier, our dataset contains light-curves with a small number of measurements scattered unevenly over large baselines. A periodogram of the typical spectral window function for our data is shown in Figure 10. There is significant power in the peaks around 1.0, ~ 7.0 , and ~ 30.0 days and their aliases, which are related to the three main duty cycles present in the SN Survey dataset. Fortunately, string length period-finding algorithms are relatively insensitive to these cycles (as evidenced by Figure 9), but objects with periods close to the periods of these cycles suffer from severe aliasing, making it difficult to distinguish between the many likely periods. We also face the challenge of insufficient sampling near points of maximum variation in light-curves; for example, eclipsing binary candidates that do not have light-curve points that sample primary and secondary eclipses will suffer from ambiguity in period determination. Finally, objects that have large photometric noise even in their differential magnitude light-curves, such as faint red stars, will return many different string lengths that do not correspond to any ‘smooth’ phased light-curve, thus making it impossible to determine their periods, even if evidence of periodicity is apparent in these objects’ unphased light-curves.

4. The RA 0 h to 4 h Light-curve Catalog

4.1. General Properties and Classification

The first release of our catalog covers the right ascension range 0 to 4 h. In this region, there are 495,797 objects extracted from the SDSS dataset as described in Section 2 above. We restrict our attention to only those objects with at least 10 observations, and process these through our ensemble photometry pipeline discussed in Section 2.3. The resulting light-curve catalog contains 365,086 point sources. We then remove objects that have large

errors in color: $\sigma(u - g) > 0.2$, $\sigma(g - r) > 0.2$, $\sigma(r - i) > 0.2$, and $\sigma(i - z) > 0.2$. This pruning leaves 228,056 objects. The SDSS imaging pipeline (see Lupton et al. 2002 and Lupton et al. 2001) efficiently separates stars and galaxies up to $r = 21.5$ mag. To minimize the contamination fraction of galaxies in our sample, but at the same time remain sensitive to faint red variables, we impose a faint magnitude limit of $r = 22.0$ mag on the objects in our light-curve catalog. This leaves us with a final catalog of 221,842 objects to consider for variability analysis.

We then classify the objects in this light-curve catalog by color-selection and cross-matching against other catalogs as discussed in Section 2.4. The results of this process are shown in Table 3. M-dwarfs make up the largest fraction of point sources by number; partly due to the initial single magnitude cutoff imposed at $z = 21.0$ mag (see Section 2), and partly because of the intrinsic frequency of these low mass stars in the Galaxy. These objects are, therefore, overrepresented in our catalog to a significant degree. We also cross-match 4,196 objects classified as QSOs by Schneider et al. (2007), 419 spectroscopically confirmed white dwarfs, and 15 hot subdwarfs from the catalog of Eisenstein et al. (2006). 165,591 point sources in our catalog are successfully cross-matched to objects classified as standard star candidates in Ivezić et al. (2007). Finally, we recover 3,972 objects classified as Stripe 82 variable candidates by Sesar et al. (2007).

Our variable extraction routines produce 6,860 ($\sim 3.1\%$ of the total objects) tentative variable candidates, and a final list of 6,520 ($\sim 2.9\%$ of the total objects) probable variable candidates in our dataset. Figure 11 (left panel) presents the variable fraction as a function of SDSS r magnitude. This fraction rises to a maximum of $\sim 4.5\%$ at the level of ~ 0.05 mag for the bin $20.0 < r \leq 21.0$, which contains a significant number of point sources. The fall in the variability fraction observed in the bin $21.0 < r \leq 22.0$ reflects the effect of increasing photometric noise on the determination of variability. In this magnitude bin, correlated variability across several bands is difficult to detect, thus the Stetson index trends towards zero, leading to a corresponding decrease in the variability fraction. Overall, we find that $\sim 2.9\%$ of the point sources in our dataset show variability at the level of ~ 0.05 mag, given a median r magnitude of ~ 19.9 . The right panel of Figure 11 shows the trends of the differential r light-curve standard deviation with median SDSS r light-curve magnitude for nonvariable (solid line) and probable variable (dashed line) objects respectively. The large difference between the two for all magnitude bins indicates that variables are robustly selected by our methods over this range of magnitudes.

Figure 12 shows a $g - r/u - g$ color-color diagram for all point sources (left panel) and just the variable candidate point sources (right panel) in our final light-curve catalog. We can place all detected sources into six broad classification regions as depicted in this figure.

Region A is where white dwarfs lie in $g - r/u - g$ color space, owing to their blue colors. Low-redshift quasars cluster in region B, also due to their blue colors. Region C contains A main sequence stars, blue horizontal branch stars, as well as blue stragglers. Region D includes mostly quasars with high redshifts ($z > 3.0$) as identified by cross-matching with the SDSS Quasar Catalog. Region E is the main stellar locus, with stars getting redder in color space as their mass decreases. This results in a progression of spectral types from approximately F to early M towards the top-right corner of the color-color diagram. The lowest-mass stars (the late M dwarfs), brown dwarfs, and other faint red objects with unreliable $u - g$ colors are found in region F. Their $u - g$ colors are unreliable due to the large photometric error in these bluer bands caused by the very red spectral energy distributions of these objects.

The right panel of Figure 12 shows the $g - r/u - g$ color distribution of 6,520 probable variable candidates. The two dominant classes of variables appear to be the QSOs in region B, and a significant amount of faint red objects present along the stellar locus in region E. We note here that the majority of variable objects classified as ‘unknown’ in Table 3 are located within the color space defined by region B, and thus are themselves likely to be QSOs. We discuss these further in Section 4.5.

We identify 143 periodic variables among the 6,520 probable variable candidates extracted from the catalog. Of these, 12 appear to show periodic variability upon inspection of their *unphased* light-curves, but have extremely poor phase coverage or too much photometric noise to allow any period to be determined and assigned to the object. Thirty more objects, most of which are mid to late M-dwarfs, show eclipse-like periodic variability, but have ambiguous periods or phased light-curves that do not show convincing periodicity upon closer inspection⁹. Figure 13 shows light-curves of a sample of 6 such problematic objects. We remove these 30 objects as well as the 12 that have no assigned periods from any further consideration.

We are finally left with 101 periodic variables identified from our light-curve catalog. Table 4 lists these objects as classified by the shape of their light-curves. The positions of these periodic variables in $u - g/g - r$ color space are shown in Figure 14. All of these objects are found on the stellar locus, and range in spectral type from A to late M. The RR Lyrae and Delta Scuti candidates are clustered in region C, where the blue horizontal branch stars may be found, as expected. In contrast, we find eclipsing variables all along the stellar locus. No periodic variables are found among the cross-matched white dwarfs or QSOs.

⁹A list of these is available from <http://shrike.pha.jhu.edu/stripe82-variables>

4.2. Variable Detection and Period Recovery Efficiency

We test our general variable identification process by constructing a synthetic light-curve catalog representative of the objects present in our dataset. Running this light-curve catalog through our ensemble photometry, variable extraction, and period finding routines then provides upper limits for the efficiency and reliability of our detection methodology. We first draw median light-curve magnitudes, the associated standard deviations, the number, and dates (MJD) of observations for each object from probability distributions matching the observed distributions of these quantities. Light-curve measurements are then perturbed using Gaussian noise appropriate for the objects’ assigned magnitudes obtained from the observed magnitude- σ relation (for example, Figure 4). A catalog of 46,000 synthetic objects covering an area of 5 degrees in right ascension and 2.5 degrees in declination is constructed using these distributions and serves as a ‘background’ for ensemble photometry of two classes of objects: sinusoidal variables and completely nonvariable objects. We insert 2,000 objects of each type into the synthetic light-curve catalog, making for a total of 50,000 objects that are then processed through our pipeline exactly in the same manner as real objects from the Stripe 82 dataset.

The 2,000 artificial sinusoidal variables are inserted into the light-curve catalog at uniform random spatial coordinates, thus distributing them evenly over the 12.5 square degree area under consideration. Periods for these objects are chosen from a uniform distribution in $\log P$ (where P is the period in days) ranging from 0.1 to 100.0 days. Amplitudes are assigned to these objects from a uniform random distribution ranging from 0.01 to 0.50 magnitudes. We simplify matters by assuming the same variability amplitude for each band. The epoch of minimum light for each periodic variable is also chosen from a uniform random distribution of observation dates present in the dataset. We then generate sinusoidally variable magnitude measurements distributed over the assigned observation dates using the periods, amplitudes, and epochs of minimum light thus chosen. Finally, each object’s assigned magnitudes are perturbed by an amount chosen from a Gaussian distribution centered at 0.0 and with a standard deviation equal to the assigned artificial light-curve standard deviation, thus introducing ‘noise’ to the light-curves of each object.

Objects are required to have at least 10 observations in their timeseries to be eligible for ensemble photometry; 1,587 of the inserted variables survive this cut. Objects with color errors greater than 0.2 and magnitudes fainter than $r = 22.0$ mag are then discarded as in our usual processing. We then run ensemble photometry and variable object extraction routines on the remaining objects. This leaves us with 1,393 objects to extract variables from. The results of these routines are summarized in Table 5. The pipeline identifies 1,101 objects as *tentative variables*; 1,091 of these are eventually tagged as *probable variables*, resulting in an

overall (ideal case) variable recovery rate of $\sim 78.3\%$. The variable extraction procedures are most efficient at brighter magnitudes (reaching maximum efficiency near $r \sim 18.5$). They become progressively less so with fainter magnitudes, due to increasing photometric noise that makes it more difficult to identify variability.

The final step in characterizing the efficiency of variable extraction is to test the recovery of the assigned periods for these sinusoidal variables. We carry this out by running all detected synthetic probable variables through our period finding routines as described in Section 3.2. We expect the recovery rate here to be quite low, given the limited phase coverage and small number of observations of each object. A periodic variable is considered to be recovered with the correct period if the difference between the recovered period and the original assigned period is less than 0.001 days. Larger differences introduce significant phasing errors when one attempts to construct phased light-curves for these objects. Overall, 600 out of 1,091 artificial sinusoidal probable variables have their periods recovered successfully, resulting in a recovery efficiency of $\sim 54.9\%$. Figure 15 shows how this recovery fraction behaves as a function of median r magnitude (top left), number of observations (top right), variability amplitude (bottom left), and input period (bottom right). The period of the variable object and the number of observations determine the phase coverage, and affect the period recovery fraction the most. Long period variables have poor phase coverage and a correspondingly small recovery fraction. The fraction drops with increasing magnitude, as expected, due to the increasing noise in the light-curves that makes it difficult to phase them correctly. The variable recovery fraction generally increases with the number of observations, except for the last few bins where the trend becomes ambiguous due to the small number of objects in these bins.

Using results from our simulations, we can also address the question of how our period finding algorithms fail when they do. Figure 16 shows the relation between the assigned input periods and the actual recovered periods for all 1,091 artificial periodic variables identified by our pipeline. The curves depict the three most common types of aliases for our periods present in this dataset. We see that in most cases, the recovered period corresponds closely to the input period, but there are significant numbers of cases where the period finding algorithms latch on to these aliases in lieu of the actual input period. This is mostly a function of the phase coverage on each variable object; the better the balance between an object’s period and the number of its observations, the more likely it is that we will recover the correct period.

We see this effect most clearly in our sample of actual eclipsing binary candidates identified from Stripe 82 data, where we discard nearly half of our initial sample due to ambiguous period recovery before settling on a final sample of 30 objects. The rapid changes in these

objects’ light-curves near eclipse and the very small amount of time each object spends in eclipse cause significant difficulties for our period finding algorithms. A photometric followup campaign to better characterize these objects would therefore be most successful if it used ephemerides generated using the periods reported here as well as several harmonics of these periods.

Finally, we inject 2,000 artificial completely nonvariable objects into the synthetic light-curve catalog. These objects only have Gaussian noise added to their light-curves, but otherwise show no trends over time. These are used to test the false positive variable identification rate of our pipeline. 1,578 such objects survive the initial ensemble pipeline cut on number of observations, while 1,399 of these survive our additional cuts on the color errors and imposed r magnitude limit. Running the pipeline on these remaining objects yields 12 objects tagged as *tentative variables*; only 2 of these are subsequently identified as *probable variables*. Neither of these remaining objects appear to have to have any periodicity, as expected. On average, therefore, $\sim 0.15\%$ of all artificial nonvariable objects inserted into the catalog are expected to be misidentified as actual variables. The actual false positive rate will be higher than this number, but we believe our pipeline separates variables from nonvariables efficiently, based on the evidence from these simulations. We expect the contamination fraction of such falsely tagged nonvariable objects in our variable sample to be, at worst, near 10%.

4.3. Obtaining the Light-curve Catalogs

A complete set of light-curves for the 6,520 variable candidates, lists of the different types of periodic variables identified here, catalogs of the objects discussed in the following sections, and finally, summary files describing all 221,842 point sources in this dataset, are available at the following website:

<http://shrike.pha.jhu.edu/stripe82-variables/>

All object catalogs are in standard FITS binary table format. Light-curves are provided as individual FITS tables, CSV, and PDF files associated with each variable object, and include various related diagnostics. Details on the format and content of these data files are available at the website mentioned above. Finally, the software code and programs used to construct our light-curve catalog and carry out ensemble photometry are also provided.

4.4. Periodic Variables

4.4.1. *Eclipsing and Ellipsoidal Binary Candidates*

We find 30 eclipsing binary candidates in our dataset. The period distribution for all of these objects is shown in the form of a histogram in Figure 17. Example light-curves for these objects are presented in Figure 18, and a listing of all eclipsing binary candidates found by our pipeline is presented in Table 6. The comments column in that table indicates the type of object as classified by its color, as well as noteworthy features of its light-curve. Objects with periods greater than 1.0 day are relatively scarce. This is primarily due to the sampling cadence of the survey. Objects with longer periods spend little time in either primary or secondary eclipse, and sparse, uneven sampling of their light-curves, coupled with a small number of observations makes it difficult to obtain unambiguous periods. In contrast, objects with small periods are more suited to our sampling cadence; these are more likely to be in eclipse at any one time, and thus provide a better estimate of the period. The abundance of short period objects, therefore, is a result of observational bias, and cannot be ascribed to physical reasons.

The binary candidates appear to be rather diverse in their nature. We find at least five W UMa type contact binary systems; two good examples of these are objects MB5010 (SDSS J035138.50-003924.5) and MB6467 (SDSS J031021.22+001453.9) in Figure 18. Object MB23368 (see Figure 18; SDSS J025953.33-004400.3) is a very short period late M-dwarf binary candidate, which shows an interesting out of eclipse variation in its light-curves, most prominently in the g and r band. This may be evidence of a star spot rotating in and out of view, but a more densely sampled light-curve for this object is required for confirmation.

Other interesting binary candidates include objects MB42018 (SDSS J032515.05-010239.7) and MB14172 (SDSS J024255.78-001551.5). MB42018 is a mid M-dwarf object that appears to have a short period and rather shallow eclipses (~ 0.3 mag for the primary, ~ 0.1 mag for the secondary), indicating a possible low mass companion. We note, however, that there is a third star present near the eclipsing binary candidate (within $1.0''$) and this may instead indicate that the shallow eclipses are caused by blended light from this system. At the other end of the size scale, MB14172 is a blue star with a long period and a deep primary eclipse and a much shallower secondary eclipse. It is tagged as a low-metallicity object and possibly a giant star by our pipeline, perhaps indicating a giant-dwarf binary system. Finally, we point out the well-sampled light-curve of the object MB8125 (SDSS J030753.52+005013.0, a short period K dwarf eclipsing binary candidate) as an example of the accuracy in period finding possible even with a relatively small number of observations (115 in this case) over the ten year length of the survey. Light-curves of all three objects are shown in Figure 18.

We note here that, in addition to the newly discovered binaries described above, we have also recovered two confirmed low mass eclipsing binaries present in the footprint of Stripe 82: the objects 2MASS J01542930+0053266 (Becker et al. 2008; M0+M1), and SDSS J031823.88-010018.4 (also known as SDSS-MEB-1; Blake et al. 2008; M4). We were, however, unable to recover the periods of these objects as reported in the literature, because of limited phase coverage and a small number of observations, but our variable identification method was sufficient to pick out these objects as obvious variable candidates. These two objects are listed in Table 6, along with our own eclipsing binary candidates.

The poor phase coverage of most of our light-curve catalog, especially for our eclipsing binary candidates, precludes detailed analysis of these objects at this point. Dedicated photometric and spectroscopic followup will be required to draw meaningful conclusions about their physical properties as derived from their light-curves. We will discuss results of such followup for some of these binary candidates in a future paper.

4.4.2. *RR Lyrae and Delta Scuti Variables*

We find 71 sinusoidal variables in our dataset. These are distinguished from the eclipsing binaries discussed previously by inspection of their phased differential magnitude light-curves. These variables can be further classified into three broad types based on light-curve shape, period, and amplitude; the RRab RR Lyrae, the RRC RR Lyrae, and high amplitude Delta Scuti variables. We fit Fourier components to the light-curves of all 71 sinusoidal variables to robustly classify them as belonging to one of the three sinusoidal variable types, thus

$$f(t) = A_0 + \sum_{k=1}^N A_k \sin [k\omega(t - t_0) + \phi_k] \quad (17)$$

where A_0 is the mean magnitude, A_k is the amplitude of the k th Fourier term, ω is the angular frequency and is given by $\omega = 2\pi/P$ for a period P , t_0 is the epoch, and ϕ_k is the phase for the k th Fourier term. We restrict the maximum order of the fit N to 3, because of the low number of observations per object, which gives us poor phase coverage. We then calculate the Fourier parameters R_{21} and ϕ_{21} , given by the respective relations

$$R_{21} = \frac{A_2}{A_1} \text{ and } \phi_{21} = \phi_2 - 2\phi_1. \quad (18)$$

The calculation of these two parameters allows us to quantitatively distinguish between RRab, RRC, and Delta Scuti variables (Poretti 2001). We further require that an object be fit successfully using Fourier components to be classified as either one of these three sinusoidal variable types and be accepted as such into our periodic variable catalog. Figure

19 shows plots of R_{21} against period (left panel) and ϕ_{21} against period. The three classes of sinusoidal variable separate cleanly in both diagrams.

There are 55 RR Lyrae variables identified during this process. Of these, 36 are of the subtype RRab, and 19 are of the subtype RRc. Table 7 gives a listing of these objects, their median SDSS light-curve magnitudes, and their periods. The periods for the RRab variables range between ~ 0.476 and ~ 0.709 days, with a median period of ~ 0.608 days. These objects show the expected trend of decreasing amplitude of variation and more symmetric light-curves with increasing period. This trend is apparent in Figure 20, which presents *gri* differential magnitude light-curves of a sample of RRab variables identified in this dataset. The 19 identified RRc variables have periods ranging from ~ 0.201 to ~ 0.409 days, with a median period of ~ 0.301 days. Figure 21 presents example *gri* differential magnitude light-curves for these objects.

Although the selection of RR Lyrae by light-curve shape and period is more robust than selection by color alone, the completeness of our sample of such objects suffers due to poor phase coverage. The 55 objects selected for our sample are a meagre fraction of the 125 RR Lyrae probable variable candidates selected by color, and an even smaller fraction of the 1,664 RR Lyrae selected by color alone without regard to their variability. We quantify the completeness and efficiency of our selection process by carrying out simulations similar to those discussed in Section 4.2.

We generate 2,000 RRab and 2,000 RRc synthetic objects using the magnitude, magnitude error, number of observations, and observation date distributions present in our dataset. Colors are assigned to these objects using the RR Lyrae candidate color cuts described in Section 2.4 and Ivezić et al. (2007). Periods are assigned to the RRab objects from a uniform distribution of periods between 0.5 and 0.8 days, and to the RRc objects from a uniform distribution of periods between 0.2 and 0.5 days. Similarly, we assign variability amplitudes from uniform distributions of amplitudes between 0.4 and 1.0 mag for RRab, and 0.1 to 0.5 mag for RRc objects respectively. Light-curves for these objects are generated and they are then inserted into separate catalogs of 48,000 nonvariable synthetic objects each, and then run through the ensemble photometry and variable extraction routines. We test the recovery of these artificial variables in two steps: (1) extracting them as *tentative* and subsequently as *probable* variables by using our variable identification methods, and (2) recovering their assigned periods by using our period finding algorithms.

Of the 2,000 synthetic RRab variables inserted into the catalog, 1,533 survive the ensemble process and subsequent conditions on color errors and magnitude limit. Of these objects, 1,517 ($\sim 98.9\%$) are successfully identified first as *tentative variables* and then as *probable variables*. Overall, 1,312 of these variables are recovered with the correct periods, making

for an average recovery fraction of $\sim 86.4\%$. Figure 22 shows the trend of the period recovery fraction with g magnitude, number of observations, amplitude, and period for synthetic RRab variables (solid lines) as well as RRC variables (dashed lines). Period recovery quickly becomes more successful as the number of observations for a given object are increased, indicating the important role of good phase coverage. The recovery rate appears to be relatively insensitive to object magnitude, discounting the objects in the brightest magnitude bin, which are much fewer in number compared to those in the other magnitude bins. The period recovery fraction also appears to be insensitive to the variability amplitude; RRab variables have amplitudes that are large compared to our survey’s sensitivity to variability. The weak trend with period is reflective of the small period range being explored.

In contrast to the high variable recovery rate of synthetic RRab variables, the synthetic RRC variables suffer due to their small variability amplitudes. Of the 2,000 such objects inserted into the catalog, 1,543 survive to the variability analysis stage after cuts on color error and magnitude limits. Only 1,132 of these objects are picked up as *tentative variables*, and subsequently as *probable variables*, resulting in a relatively poor variable recovery rate of 73.4%. The variable recovery rate shows a significant decreasing trend with fainter magnitude after peaking in the magnitude bin $19.0 < g \leq 20.0$, similar to the results of general variable recovery simulations presented in Section 4.2. The period recovery rate for synthetic RRC variables is similar to that for synthetic RRab variables: 934 of 1,132 of these ($\sim 82.5\%$) are recovered with the correct periods. Figure 22 (dashed lines) shows how this rate is related to various input parameters. Once again, the most important factor is the number of observations, and by extension, the phase coverage for our variable objects.

Given the results of the variable and period recovery simulations above, we estimate a completeness of no better than 65% for our RR Lyrae sample. Although this is low, the objects that are discovered are very likely to be real RRab and RRC variables due to successful classification by light-curve shape, period, and Fourier decomposition. We can, therefore, attempt to trace halo substructure using these objects for illustrative purposes. Assuming an absolute magnitude $M_V = 0.7$ for RR Lyrae stars, we calculate the distances to the 55 such objects in our catalog. Figure 23 shows a plot of the distribution of these RR Lyrae (36 RRab, and 19 RRC) as a function of the distance and the right ascension. The large clump near 25 kpc and ranging from 30° to 40° in right ascension is associated with part of the Sagittarius dwarf stream (S167-54-21.5 in Newberg et al. 2002). Other clumps can be seen in the spatial distribution plot, and these may be associated with halo substructure as well. A detailed examination of RR Lyrae in Stripe 82 and how they relate to Milky Way substructure at large distances is, however, beyond the scope of this work, largely due to the small number of RR Lyrae in our sample. Excellent treatments of these topics may be instead be found in de Lee (2008) and Watkins et al. (2009).

The final class of sinusoidal variables we discuss are the high amplitude Delta Scuti (HADS) variables. These have short periods (< 0.3 days) and amplitudes (up to 0.5 mag) greater than those of the usual Delta Scuti stars. We find 16 candidates for such objects in our dataset. Table 8 gives a listing of these, along with median light-curve magnitudes and periods. Figure 24 shows example light-curves for 6 of these objects. The median period for these objects is ~ 0.063 days, with a minimum period of ~ 0.050 days, and a maximum period of ~ 0.093 days. Longer period HADS variables can potentially be confused with short period RRc RR Lyrae in both period and color space (see Figure 14), however, Fourier decomposition provides a robust mechanism of distinguishing between the two kinds of variables, as seen in Figure 19.

4.5. Variable Quasars

The vast majority of quasars are expected to be variable on both short and long timescales (see Hawkins 2002, de Vries et al. 2003, and references therein). The short term variability of these objects is likely to be associated with eruptive events and manifests as large-amplitude variations in light-curves (for example, BL Lac type objects). In contrast, the long term variability of quasars is dominated by small-amplitude variability, often resulting in increasing or decreasing trends in brightness on multi-year timescales. It is possible to use this intrinsic variability to distinguish between objects on the stellar locus and quasars (Sesar et al. 2007, and references therein).

Our light-curve catalog contains 4,196 quasars matched to the SDSS Quasar Catalog (Schneider et al. 2007). These objects mostly fall within regions B and D of the $g - r/u - g$ color-color diagram (see Figure 12, left panel). The objects in the quasar catalog were selected using SDSS photometry and spectra and have measured redshifts available. We identify 2,704 objects among these matched quasars as probable variables tagged by our pipeline (see Figure 25 for example light-curves), resulting in a variable fraction of ~ 0.64 . Furthermore, these variable quasars make up a sizeable fraction, ~ 0.41 , of all identified candidate variable sources.

New QSO candidates in our sample may be identified by taking advantage of their intrinsic variability and non-stellar colors. As noted in Section 4.1, there are 8,463 objects tagged as ‘unknown’ in our catalog due to the lack of any corresponding objects in any other catalogs, as well as no classification possible by SDSS color alone. Of these objects, 1,102 are tagged as probable variables. A large fraction of these probable variable ‘unknown’ objects have non-stellar colors and may be found in region A of Figure 12 (left panel). We identify new quasar candidates by requiring that they be tagged as probable variables and satisfy

either one of two color cuts: low- z quasars using $-0.3 < u - g < 0.7$ and $-0.3 < g - r < 0.5$, and high- z quasars using $u - g > 1.4$ and $u - g > 1.6(g - r) + 1.34$. These color and variability cuts result in the identification of 2,403 QSO candidates.

Figure 26 (left panel) shows the relation between Stetson indices J_{ug} and J_{ri} for variable QSOs matched to the SDSS Quasar Catalog and stellar locus objects. Quasars appear to be more strongly variable at shorter wavelengths (Vanden Berk et al. 2004), and this tendency shows up in slopes of the J_{ug} vs J_{ri} trends plotted in the figure. Variable stellar locus objects show most of their variability at longer wavelengths, and thus have larger relative J_{gr} , and J_{ri} values. The addition of 2,403 variable QSO candidates identified by our color and variability cuts to the plot (Figure 26, right panel) does not appreciably change the slopes of the two distributions, indicating that these objects largely follow the trend for matched QSOs from the SDSS Quasar Catalog.

Despite these candidate objects matching the colors of, as well having similar variability properties to the already known QSOs, confirmation of their quasar nature would require an extensive spectroscopic campaign. Lists of all objects matched to the SDSS Quasar Catalog, as well as those objects identified as candidate QSOs here are both available from the website mentioned in Section 4.1 above.

4.6. Nonvariable Objects

There are 214,982 objects in the final light-curve catalog (the $r < 22.0$ sample) that fail to meet the selection criteria for *tentative variables*. Not all of these will be actual nonvariables. We can, however, use the tools developed here to define a sample of point sources that show no variability at the limits of our sensitivity. *Probable nonvariables* are thus selected if they: (1) are not tagged as tentative variables by our pipeline, (2) do not match to any objects in the SDSS-I variable star catalog (Sesar et al. 2007), (3) have a match in the SDSS standard star catalog (Ivezić et al. 2007), (4) do not match to any objects in the SDSS quasar catalog (Schneider et al. 2007), and finally, (5) have Stetson variability indices J_{ug} , J_{gr} , J_{ri} , and J_{iz} all less than 0.05. These conditions select 19,704 objects. A further refinement can be made by demanding that these objects have at least 50 detections each, ensuring that the Stetson index selection for nonvariability is valid over at least three years of observations. With this final criterion in place, the probable nonvariable sample consists of 11,328 point sources.

Figure 27 shows a $g - r / u - g$ color-color diagram of these objects. Nearly all of them are found on the stellar locus and are well-distributed in color from blue A stars to red M

stars. These objects form a subset of the sources found in the SDSS standard star catalog and have been selected as nonvariables using a much longer timeseries baseline. Additional high cadence photometric monitoring would be required to rule out variability below the level of what we can detect with our methods ($\sigma \leq 0.05$ mag) before these are actually deemed suitable for use in a canonical standard star catalog. A list of these stars is available from this paper’s accompanying website.

5. Conclusions

We have constructed a light-curve catalog of 221,842 point sources in the RA 0 to 4 h half of Stripe 82, and identified 6,520 candidate variables. Of these, 2,704 turned out to be already identified quasars, while another 2,403 were classified as QSO candidates due to their colors and variability properties. We found 101 periodic variables in this dataset, including 30 candidate eclipsing binary systems, 55 RR Lyrae and 16 high amplitude Delta Scuti candidates. We also identified a sample of 11,328 point sources that do not appear to be variable, based on observations over a long time baseline and rejection from our variable extraction algorithms.

The use of inhomogeneous ensemble differential photometry and the Stetson variability index was crucial in identifying possible variables among the objects in the dataset, while removing many sources that appeared to be falsely variable. The poor phase coverage of our light-curves presented difficulties in extracting periodic variables from the candidate variable sources. Binless phase dispersion minimization methods, such as the Dworetzky and Stetson string length algorithms worked well on our sparse and unevenly sampled data, and had the added advantage of being unbiased with respect to the kind of variability being probed.

We have made public our Stripe 82 variable object light-curve catalog, along with the software implementation of our ensemble photometry pipeline. In an upcoming paper, we will address variability in the remaining half of Stripe 82 (RA 20 to 0 h), and present our final catalogs for periodic and other types of variables present in this dataset. Unfortunately, the relative faintness of many interesting periodic variables, especially the binary candidates, presents difficulties in the confirmation of their nature and further study of their properties. We believe, however, that this dataset will be an important resource for variability studies of a large and diverse array of objects, serving as a prototype in advance of future large synoptic surveys such as Pan-STARRS and LSST.

This research was supported by NASA grant NAG5-7697. We gratefully acknowledge the assistance of Brian Yanny (FNAL) and Ani Thakar (JHU) in accessing and downloading

the SDSS-II Supernova Survey data. W. A. B. would like to thank Arti Garg (LLNL), Mark Huber (JHU), and Suvi Gezari (JHU) for useful discussions. We thank the anonymous referee for their careful reading and helpful comments and suggestions, which greatly improved the manuscript. This research has made extensive use of the IDL Astronomy Library and the University of Michigan/Chicago/NYU SDSS IDL Library. Finally, we acknowledge the use of data from the Sloan Digital Sky Survey (SDSS) and SDSS-II.

Funding for the SDSS and SDSS-II has been provided by the Alfred P. Sloan Foundation, the Participating Institutions, the National Science Foundation, the U.S. Department of Energy, the National Aeronautics and Space Administration, the Japanese Monbukagakusho, the Max Planck Society, and the Higher Education Funding Council for England. The SDSS Web Site is <http://www.sdss.org/>

The SDSS is managed by the Astrophysical Research Consortium for the Participating Institutions. The Participating Institutions are the American Museum of Natural History, Astrophysical Institute Potsdam, University of Basel, University of Cambridge, Case Western Reserve University, University of Chicago, Drexel University, Fermilab, the Institute for Advanced Study, the Japan Participation Group, Johns Hopkins University, the Joint Institute for Nuclear Astrophysics, the Kavli Institute for Particle Astrophysics and Cosmology, the Korean Scientist Group, the Chinese Academy of Sciences (LAMOST), Los Alamos National Laboratory, the Max-Planck-Institute for Astronomy (MPIA), the Max-Planck-Institute for Astrophysics (MPA), New Mexico State University, Ohio State University, University of Pittsburgh, University of Portsmouth, Princeton University, the United States Naval Observatory, and the University of Washington.

REFERENCES

- Alcock, C., et al. 2001, *ApJS*, 136, 439
- Alonso, R., et al. 2004, *ApJ*, 613, L153
- Bakos, G. Á., Lázár, J., Papp, I., Sári, P., & Green, E. M. 2002, *PASP*, 114, 974
- Becker, A. C., et al. 2008, *MNRAS*, 386, 416
- Blake, C. H., Torres, G., Bloom, J. S., & Gaudi, B. S. 2008, *ApJ*, 684, 635
- Bramich, D. M., et al. 2008, *MNRAS*, 386, 887
- de Lee, N. 2008, Ph.D. Thesis, Michigan State University

- de Vries, W. H., Becker, R. H., & White, R. L. 2003, *AJ*, 126, 1217
- Dworetsky, M. M. 1983, *MNRAS*, 203, 917
- Eisenstein, D. J., et al. 2006, *ApJS*, 167, 40
- Frieman, J. A., et al. 2008, *AJ*, 135, 338
- Gunn, J. E., et al. 2006, *AJ*, 131, 2332
- Hawkins, M. R. S. 2002, *MNRAS*, 329, 76
- Hogg, D. W., Finkbeiner, D. P., Schlegel, D. J., & Gunn, J. E. 2001, *AJ*, 122, 2129
- Honeycutt, R. K. 1992, *PASP*, 104, 435
- Ivezić, Ž., et al. 2007, *AJ*, 134, 973
- Ivezic, Z., et al. 2008, arXiv:0805.2366
- Kaiser, N., et al. 2002, *Proc. SPIE*, 4836, 154
- Kovács, G., Zucker, S., & Mazeh, T. 2002, *A&A*, 391, 369
- Kowalski, A. F., Hawley, S. L., Hilton, E. J., Becker, A. C., West, A. A., Bochanski, J. J., & Sesar, B. 2009, *AJ*, 138, 633
- Lafier, J., & Kinman, T. D. 1965, *ApJS*, 11, 216
- Lupton, R. H., Ivezic, Z., Gunn, J. E., Knapp, G., Strauss, M. A., & Yasuda, N. 2002, *Proc. SPIE*, 4836, 350
- Lupton, R., Gunn, J. E., Ivezić, Z., Knapp, G. R., & Kent, S. 2001, *Astronomical Data Analysis Software and Systems X*, 238, 269
- McCullough, P. R., et al. 2006, *ApJ*, 648, 1228
- Newberg, H. J., et al. 2002, *ApJ*, 569, 245
- Pojmanski, G. 2002, *Acta Astronomica*, 52, 397
- Pollacco, D. L., et al. 2006, *PASP*, 118, 1407
- Poretti, E. 2001, *A&A*, 371, 986
- Scargle, J. D. 1982, *ApJ*, 263, 835

- Schneider, D. P., et al. 2007, *AJ*, 134, 102
- Sesar, B., et al. 2007, *AJ*, 134, 2236
- Skrutskie, M. F., et al. 2006, *AJ*, 131, 1163
- Stetson, P. B. 1996, *PASP*, 108, 851
- Sullivan, M., & The Supernova Legacy Survey Collaboration 2005, 1604-2004: Supernovae as Cosmological Lighthouses, 342, 466
- Schwarzenberg-Czerny, A. 1989, *MNRAS*, 241, 15
- Stoughton, C., et al. 2002, *AJ*, 123, 485
- Tyson, J. A. 2002, *Proc. SPIE*, 4836, 10
- Udalski, A., et al. 2002, *Acta Astronomica*, 52, 1
- Vanden Berk, D. E., et al. 2004, *ApJ*, 601, 692
- Watkins, L. L., et al. 2009, *MNRAS*, 398, 1757
- West, A. A., et al. 2008, *AJ*, 135, 785
- Yanny, B., et al. 2009, *AJ*, 137, 4377
- York, D. G., et al. 2000, *AJ*, 120, 1579

Table 1. Data fields extracted from Stripe 82 object catalogs

tsObj FITS/CAS Database Field	Description
RUN	The SDSS run
RERUN	Version of the SDSS FRAMES pipeline (40 or 41 in our dataset)
CAMCOL	CCD camera column (ranges from 1 to 6)
FIELD	Field number in SDSS run ($13' \times 10'$ per field)
ID	Non-unique ID number of a detection in a field
RA	Right ascension J2000 ($^{\circ}$)
DEC	Declination J2000 ($^{\circ}$)
OBJC_FLAGS/FLAGS	Quality flags associated with a detection
TYPE ^a	Detection type (3 = galaxy, 6 = star)
PARENT/PARENTID ^a	ID of parent object if current detection is a deblended child
NCHILD ^a	Number of deblended children if current detection is a blend
STATUS ^a	Status of the detection (see text for details)
PSFCOUNTS/PSFMAG	PSF fitted magnitude in <i>ugriz</i> bands
PSFCOUNTSERR/PSFMAG_ERR	Uncertainty in PSF fitted magnitude in <i>ugriz</i> bands
FIBERCOUNTS/FIBERMAG	Magnitude from flux in $3''$ fiber radius in <i>ugriz</i> bands
FIBERCOUNTSERR/FIBERMAG_ERR	Uncertainty in fiber magnitude in <i>ugriz</i> bands
MJD	MJD of detection of object in <i>ugriz</i> bands
REDDENING/EXTINCTION	Extinction in magnitudes for <i>ugriz</i> bands

^aThese fields are used to select suitable objects for extraction and are not saved in the output catalog

Table 2. Color selection algorithms for classifying point sources

Object Type	Color Selection
RR Lyrae candidate ^a	$0.98 < (u - g) < 1.30$ and $-0.05 < RR1 < 0.35$ and $0.06 < RR2 < 0.55$ and $-0.15 < (r - i) < 0.22$ and $-0.21 < (i - z) < 0.25$
Main-sequence + white-dwarf ^{fb d}	$(u - g) < 2.25$ and $-0.2 < (g - r) < 1.2$ and $0.5 < (r - i) < 2.0$ and $-19.78(r - i) + 11.13 < (g - r) < 0.95(r - i) + 0.5$
sdO/sdB/white-dwarf ^b	$-1.0 < (g - r) < -0.2$ and $-1.0 < (u - g) < 0.7$ and $u - g + 2(g - r) < -0.1$
low-metallicity ^b	$-0.5 < (g - r) < 0.75$ and $0.6 < (u - g) < 3.0$ and $l > 0.135$
AGB ^b	$2.5 < (u - g) < 3.5$ and $0.9 < (g - r) < 1.3$ and $s < -0.06$
A/blue horizontal branch ^b	$-1.0 < (u - g) < -0.2$ and $-0.5 < (g - r) < 0.2$
F/G ^b	$0.20 < (g - r) < 0.48$
F-turnoff/sdF ^b	$-0.7 < P1 < -0.25$ and $0.4 < (u - g) < 1.4$ and $-0.5 < (g - r) < 0.7$
G ^b	$0.48 < (g - r) < 0.55$
K-dwarf ^b	$0.55 < (g - r) < 0.75$
K-giant ^b	$0.7 < (u - g) < 4.0$ and $0.35 < (g - r) < 0.7$ and $0.15 < (r - i) < 0.6$ and $l > 0.07$
sdM ^b	$(g - r) > 1.6$ and $0.95 < (r - i) < 1.3$
M-dwarf ^c	$0.666 < 0.875(r - i) + 0.484[(i - z) + 0.00438] < 3.4559$
brown-dwarf ^d	$z < 19.5$ and $u > 21.0$ and $g > 22.0$ and $r > 21.0$ and $(i - z) > 1.7$

^aUsing colors from Sesar et al. (2007).

^bUsing colors from Yanny et al. (2009).

^cColor locus computed from mean M-dwarf colors in West et al. (2008).

^dUsing magnitudes that are not dereddened.

Note. — The various color indices used above are defined below:

$$P1\text{-color} = 0.91(u - g) + 0.415(g - r) - 1.28$$

$$l\text{-color} = -0.436u + 1.129g - 0.119r - 0.574i + 0.1984$$

$$s\text{-color} = -0.249u + 0.795g - 0.555r + 0.124$$

$$RR1\text{-color} = (u - g) + 0.67(g - r) - 1.07$$

$$RR2\text{-color} = 0.45(u - g) - (g - r) - 0.12$$

Table 3. Distribution of point sources by type and variability ($r < 22.0$ sample)

Object type	Probable variables	Total objects	Variable fraction
sdO/sdB/WD	4	235	0.017
A/BHB	180	1841	0.097
F-turnoff/sdF	507	26294	0.019
F/G	1333	42901	0.031
G dwarf	130	8346	0.016
K giant	141	14790	0.009
AGB	14	6001	0.002
Low-metallicity	348	13522	0.026
K dwarf	193	16141	0.012
M subdwarf	4	332	0.012
M dwarf	253	107483	0.002
brown dwarf	0	0	0.000
MS+WD	82	602	0.136
unknown ^a	1102	8463	0.130
RR Lyrae candidate ^b	125	1664	0.075
SDSS QSO ^c	2704	4196	0.644
SDSS white dwarf ^d	0	419	0.000
SDSS hot subdwarf ^d	0	15	0.000
SDSS-I variable ^e	2766	3972	0.696
SDSS standard ^f	562	165591	0.003
All point sources	6520	221842	0.029

^aNo color classification possible and no matches to other catalogs.

^bUsing color-selection from Sesar et al. (2007).

^cCross-matched to objects in Schneider et al. (2007).

^dCross-matched to objects in Eisenstein et al. (2006).

^eCross-matched to objects in Sesar et al. (2007).

^fCross-matched to objects in Ivezić et al. (2007).

Note. — Objects may have multiple types assigned, based on their colors.

Table 4. Periodic variable candidates classified by light-curve shape

Periodic variable type	Number
RR Lyrae type RRab	36
RR Lyrae type RRc	19
Delta Scuti	16
Eclipsing Binary	30
Total	101

Table 5. Recovery rates for artificial sinusoidal variables as a function of r magnitude bin

Magnitude Bin	Inserted Objects	Tentative Variables	Probable Variables	Recovery Fraction
$16.0 < r \leq 17.0$	9	6	6	0.67
$17.0 < r \leq 18.0$	103	88	88	0.85
$18.0 < r \leq 19.0$	180	158	157	0.87
$19.0 < r \leq 20.0$	303	246	245	0.81
$20.0 < r \leq 21.0$	454	362	360	0.79
$21.0 < r \leq 22.0$	344	241	235	0.68

Table 6. Eclipsing and Ellipsoidal Binary Candidates

Object	Obs.	<i>u</i>	<i>g</i>	<i>r</i>	<i>i</i>	<i>z</i>	Period [days]	Comments
SDSS J000845.39+002744.2	54	20.51	19.36	18.82	18.60	18.53	0.34419	low-metallicity
SDSS J002719.16+002400.6	47	21.04	20.08	19.74	19.61	19.58	1.31839	F/G
SDSS J002851.08+000751.0	49	22.70	20.50	19.07	18.04	17.48	0.59098	M2
SDSS J003042.11+003420.2	51	23.02	20.57	19.08	17.93	17.32	0.45705	M3
SDSS J011155.73-002633.0	34	22.37	20.57	19.94	19.71	19.55	0.22758	K dwarf, semi-detached?
SDSS J011156.52-005221.4	35	19.25	18.29	18.02	17.95	17.99	0.23002	F/G, contact?
SDSS J011302.57+004822.9	52	21.20	19.34	18.50	18.14	17.96	0.31660	F/G?
SDSS J011405.02+001138.5	44	20.78	19.88	19.67	19.62	19.64	0.28550	F/G, contact?
SDSS J013536.05-011058.7	44	20.99	20.02	19.95	19.99	20.06	0.39226	A/BHB, contact?
SDSS J015429.30+005326.7 ^a	43	21.91	19.50	18.17	17.25	16.77	2.63902	M1
SDSS J015940.01+010328.4	58	23.46	21.47	20.03	19.36	18.97	0.33779	M0
SDSS J020540.08-002227.6	57	20.39	19.42	19.16	19.10	19.12	0.79789	F/G, deep primary
SDSS J020816.51+003510.0	48	19.69	18.61	18.77	18.93	19.07	1.61420	A/BHB
SDSS J021121.55-003808.3	40	21.57	19.10	17.77	17.07	16.63	0.31210	M0
SDSS J021624.34-001817.7	45	21.95	20.80	20.43	20.34	20.28	0.63678	F/G
SDSS J022733.94+002615.2	49	20.04	18.83	18.96	19.09	19.21	0.70626	A/BHB
SDSS J022858.99-004120.4	37	20.61	19.53	19.55	19.63	19.73	0.64725	A/BHB
SDSS J023621.96+011359.1	57	19.97	19.00	18.74	18.67	18.66	0.35666	F/G, contact?
SDSS J024109.55+004813.6	52	21.27	19.29	18.31	17.90	17.64	0.27645	deep primary
SDSS J024255.78-001551.5	62	21.42	20.20	19.68	19.48	19.39	3.19764	low-metallicity, long period
SDSS J025953.33-004400.3	53	21.46	20.50	19.36	18.26	17.57	0.14418	M2, contact?
SDSS J030753.52+005013.0	115	21.84	19.74	18.75	18.34	18.12	0.35353	K dwarf, detached
SDSS J030834.42+005835.2	68	22.93	20.61	19.49	19.01	18.78	0.27080	contact?
SDSS J031002.47-000916.2	54	19.79	18.83	18.44	18.31	18.29	2.19058	F/G
SDSS J031021.22+001453.9	48	19.77	18.62	18.11	17.92	17.82	0.26684	low-metallicity, contact
SDSS J031823.88-010018.4 ^b	34	22.80	20.56	19.10	17.55	16.73	0.40704	M4
SDSS J032515.05-010239.7	48	22.22	19.86	18.39	17.42	16.87	0.39451	M2, shallow eclipses
SDSS J032949.18-001240.8	62	23.96	21.16	19.78	19.20	18.85	0.39196	M0

Table 6—Continued

Object	Obs.	<i>u</i>	<i>g</i>	<i>r</i>	<i>i</i>	<i>z</i>	Period [days]	Comments
SDSS J034256.26-000058.0	51	20.29	19.40	19.13	19.06	19.09	0.32034	F/G, semi-detached?
SDSS J034757.70-001423.5	53	20.51	19.68	19.32	19.24	19.25	0.27509	F/G
SDSS J035138.50-003924.5	54	21.03	19.07	18.18	17.88	17.70	0.19892	K/M?, contact
SDSS J035300.50+004836.0	40	22.39	20.62	19.31	18.17	17.61	0.14855	M2, ellipsoidal?

^aThis is the confirmed eclipsing binary found by Becker et al. (2008).

^bThis is the confirmed eclipsing binary found by Blake et al. (2008).

Note. — Objects are presented in order of increasing right ascension.

Table 7. RRab and RRc RR Lyrae Variables

Object	Obs.	<i>u</i>	<i>g</i>	<i>r</i>	<i>i</i>	<i>z</i>	Period [days]	Type
SDSS J000803.72-010557.9	49	20.61	19.45	19.17	19.11	19.11	0.64004	RRab
SDSS J001031.09+010132.4	43	20.21	19.06	18.87	18.81	18.76	0.33755	RRc
SDSS J001301.12-003502.6	27	19.41	18.21	17.94	17.81	17.82	0.61226	RRab
SDSS J001800.72+010424.9	33	21.40	20.41	20.26	20.21	20.19	0.53879	RRab
SDSS J003119.26+005055.8	48	20.41	19.31	19.12	19.09	19.05	0.62216	RRab
SDSS J003209.57-000445.1	26	20.52	19.40	19.42	19.48	19.62	0.20442	RRc
SDSS J003748.95-000312.0	49	20.74	19.70	19.41	19.32	19.31	0.62441	RRab
SDSS J004125.63+010859.3	14	18.65	17.53	17.39	17.41	17.48	0.25317	RRc
SDSS J004951.22-000705.8	26	20.85	19.86	19.70	19.67	19.81	0.20296	RRc
SDSS J005253.90-002141.8	27	20.37	19.30	19.03	18.95	18.92	0.58011	RRab
SDSS J005712.29-000557.7	27	19.33	18.24	18.09	18.08	18.10	0.38487	RRc
SDSS J012052.63-010411.8	46	21.10	19.93	19.68	19.62	19.56	0.58336	RRab
SDSS J012333.48+010420.7	15	18.89	17.76	17.52	17.46	17.43	0.28045	RRc
SDSS J012543.58+011032.7	43	20.51	19.45	19.42	19.45	19.57	0.20111	RRc
SDSS J012714.38+004403.6	14	18.79	17.64	17.53	17.50	17.54	0.27462	RRc
SDSS J012813.56+011357.4	28	19.12	17.94	17.70	17.63	17.59	0.58792	RRab
SDSS J013352.87-004502.7	18	18.64	17.47	17.22	17.10	17.10	0.60606	RRab
SDSS J014528.54+005133.7	47	20.17	19.14	19.11	19.17	19.24	0.22814	RRc
SDSS J015813.75+010143.5	37	19.31	18.17	17.90	17.82	17.79	0.70862	RRab
SDSS J020206.96-003534.2	34	21.97	20.84	20.61	20.53	20.39	0.59791	RRab
SDSS J020245.96-000001.7	24	18.61	17.51	17.26	17.18	17.18	0.56383	RRab
SDSS J020430.98+002005.4	19	19.12	17.95	17.89	17.83	17.82	0.63040	RRab
SDSS J020548.43+000144.4	40	19.54	18.42	18.20	18.14	18.15	0.55212	RRab
SDSS J020825.13-003444.4	35	19.68	18.58	18.35	18.30	18.26	0.51544	RRab
SDSS J022309.05+005734.2	43	19.15	18.02	17.82	17.71	17.70	0.63008	RRab
SDSS J022429.81+000725.8	34	19.44	18.38	18.20	18.16	18.16	0.47630	RRab
SDSS J022857.91+005359.8	44	19.52	18.47	18.22	18.13	18.13	0.61506	RRab
SDSS J023001.99-011146.9	39	19.55	18.43	18.16	18.11	18.11	0.64910	RRab
SDSS J023346.13-001901.7	22	19.07	17.97	17.75	17.69	17.68	0.50251	RRab
SDSS J023635.42+003005.0	44	19.65	18.49	18.24	18.17	18.16	0.53365	RRab
SDSS J023932.33+002650.0	45	19.53	18.27	18.26	18.31	18.35	0.30838	RRc
SDSS J024216.46+003438.6	52	20.30	19.27	19.28	19.35	19.41	0.20272	RRc
SDSS J024647.88+010944.7	47	20.36	19.33	19.26	19.32	19.34	0.30117	RRc
SDSS J024701.75-010814.8	20	18.72	17.64	17.48	17.49	17.51	0.21192	RRc
SDSS J024727.34-000026.1	35	20.26	19.19	19.11	19.21	19.26	0.30126	RRc
SDSS J025658.30-010918.3	43	19.09	18.03	17.76	17.70	17.69	0.51943	RRab
SDSS J025717.50+004706.9	38	19.79	18.63	18.42	18.36	18.36	0.55448	RRab

Table 7—Continued

Object	Obs.	<i>u</i>	<i>g</i>	<i>r</i>	<i>i</i>	<i>z</i>	Period [days]	Type
SDSS J025828.94-003635.1	27	19.13	18.06	17.91	17.94	17.95	0.35891	RRc
SDSS J030304.27+003029.6	53	19.47	18.34	18.11	18.03	18.07	0.64189	RRab
SDSS J030413.34+005828.1	54	19.34	18.27	18.00	17.93	17.94	0.61633	RRab
SDSS J030413.80-011314.3	19	18.37	17.31	17.19	17.15	17.17	0.36579	RRc
SDSS J031537.87-005341.9	30	19.08	17.97	17.74	17.65	17.66	0.62367	RRab
SDSS J032109.31+000705.7	31	18.99	17.86	17.62	17.53	17.51	0.56928	RRab
SDSS J032202.45-000151.6	12	21.63	20.49	20.28	20.13	20.09	0.67613	RRab
SDSS J032910.97+003614.3	55	19.51	18.32	18.10	18.09	18.11	0.34381	RRc
SDSS J032953.69-011413.0	64	20.45	19.46	19.21	19.11	19.11	0.58634	RRab
SDSS J033343.92+004457.6	32	18.95	17.84	17.62	17.56	17.59	0.40888	RRc
SDSS J033817.21-011112.9	62	20.70	19.69	19.41	19.29	19.32	0.67096	RRab
SDSS J034239.98-000009.9	74	19.33	18.25	17.99	17.91	17.93	0.61181	RRab
SDSS J034602.52-003342.2	41	19.31	18.20	18.08	18.06	18.13	0.35783	RRc
SDSS J034830.07+004042.4	39	19.68	18.57	18.34	18.27	18.24	0.61444	RRab
SDSS J034830.94-002320.9	56	19.88	18.79	18.53	18.49	18.50	0.63686	RRab
SDSS J034836.34+005334.7	53	19.48	18.42	18.13	18.07	18.08	0.58038	RRab
SDSS J034837.58+000804.8	57	19.15	18.13	17.90	17.84	17.87	0.64671	RRab
SDSS J035400.50+002110.2	32	19.02	18.01	17.76	17.71	17.73	0.58990	RRab

Note. — Objects are presented in order of increasing right ascension.

Table 8. High Amplitude Delta Scuti Variables

Object	Obs.	<i>u</i>	<i>g</i>	<i>r</i>	<i>i</i>	<i>z</i>	Period [days]
SDSS J001142.02+005946.8	42	20.13	19.17	19.05	19.05	19.09	0.06837
SDSS J001544.29+003735.1	84	20.03	18.92	18.92	18.97	19.03	0.04953
SDSS J005312.91-000522.5	37	21.14	20.19	20.10	20.13	20.21	0.06073
SDSS J013945.70-003325.6	50	20.80	19.73	19.74	19.77	19.82	0.06480
SDSS J014200.19-001756.6	49	20.70	19.64	19.58	19.65	19.72	0.06682
SDSS J014225.68+001549.6	51	20.27	19.28	19.18	19.18	19.23	0.09279
SDSS J014442.67-003741.7	94	20.55	19.57	19.54	19.55	19.54	0.06245
SDSS J014531.34+011211.9	56	20.09	19.21	19.10	19.08	19.12	0.08348
SDSS J020841.38-002038.3	50	19.60	18.57	18.49	18.54	18.62	0.06145
SDSS J021541.11-000750.1	47	20.50	19.55	19.47	19.53	19.57	0.05419
SDSS J024132.57+002324.1	37	20.27	19.28	19.18	19.21	19.25	0.06852
SDSS J024751.89-002434.5	47	21.13	20.17	20.07	20.10	20.07	0.06713
SDSS J030256.28-004150.7	41	18.84	17.86	17.82	17.87	17.93	0.05813
SDSS J030758.97+000751.7	58	20.42	19.41	19.41	19.44	19.51	0.06542
SDSS J031956.18-000238.9	49	20.00	19.01	18.96	19.00	19.08	0.05815
SDSS J034507.01+010040.1	30	21.30	20.16	20.19	20.21	20.13	0.05733

Note. — Objects are presented in order of increasing right ascension

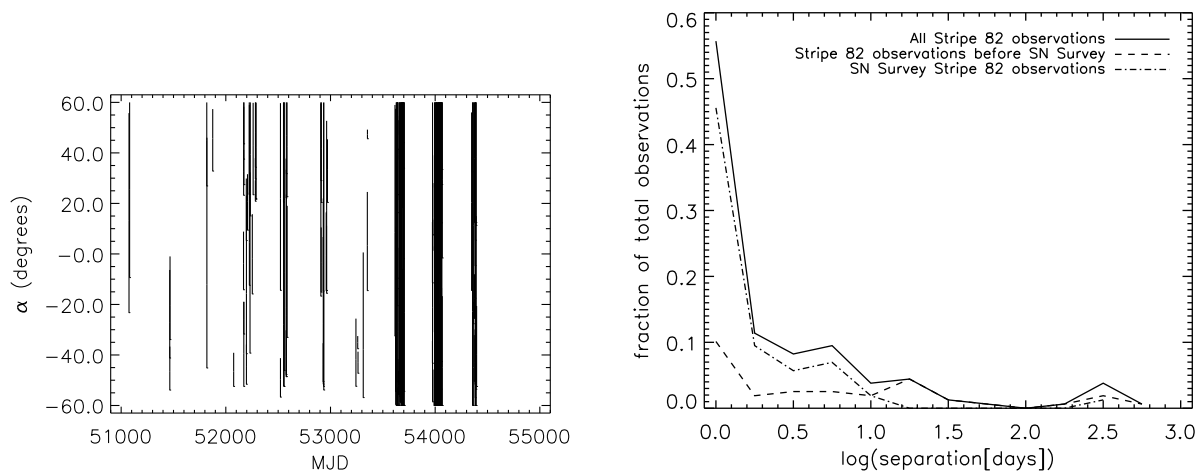


Fig. 1.— Left: Stripe 82 run temporal coverage vs. right ascension. The dense clusters at the right are the observation runs associated with the Supernova Survey. Note the large gaps between successive years of coverage of the Stripe. Right: Histogram of the separation in days between consecutive observations of Stripe 82. The bins are 0.25 dex wide. The solid line represents all observations of the Stripe; the dashed line represents observations of the Stripe before the SN Survey; the dot-dashed line represents observations of the Stripe carried out during the SN Survey. The high relative cadence of the SN Survey observations is apparent.

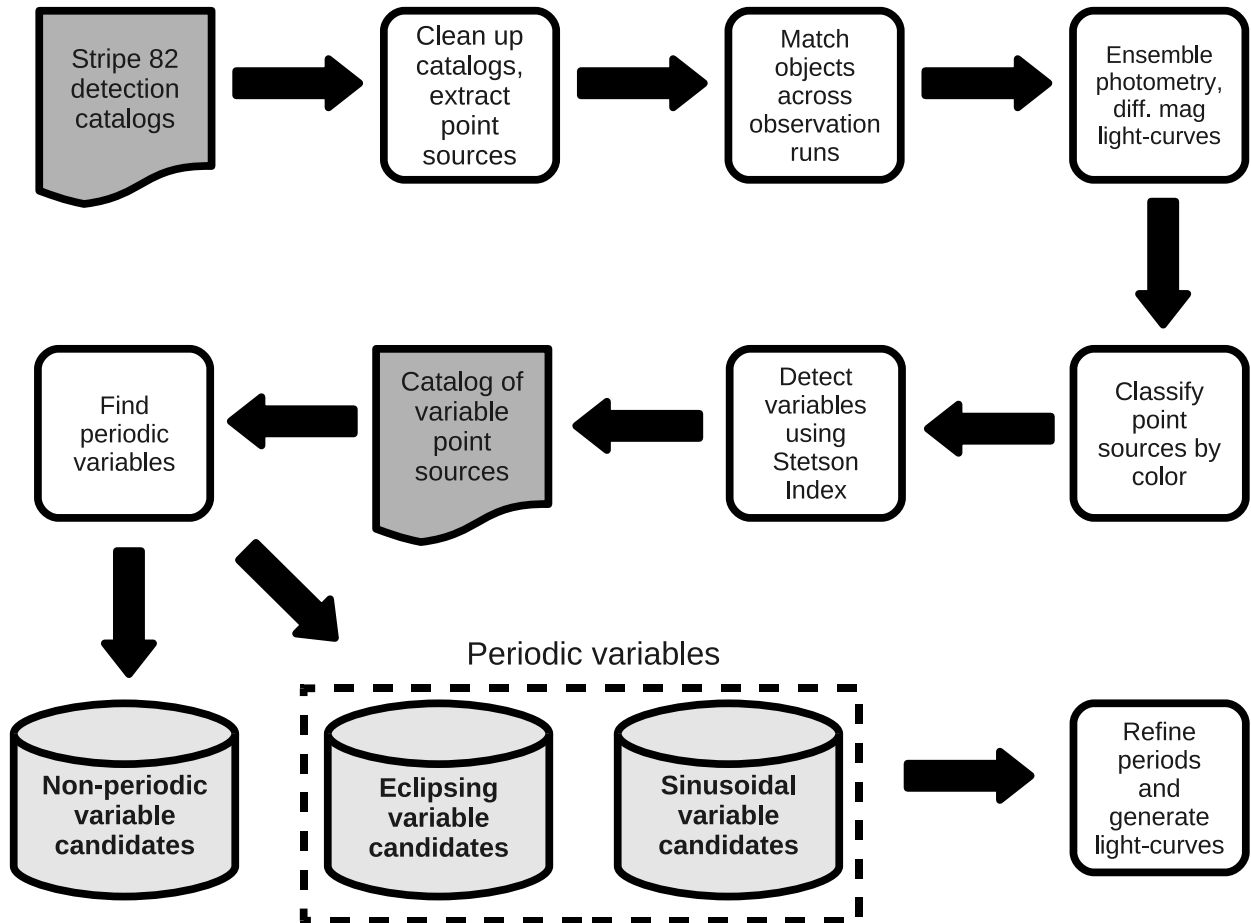


Fig. 2.— A schematic view of our processing pipeline. The initial extraction, reduction of object catalogs from the SN Survey, and ensemble photometry is described in Section 2. Variables are detected using the methods presented in Section 3.1. We find periodic variables by running the period search algorithms outlined in Section 3.2. Once these are found, we refine their periods, and generate their phased light-curves and ephemerides. Non-periodic variables include long term variables (variable on scales of years), quasars, and flare stars.

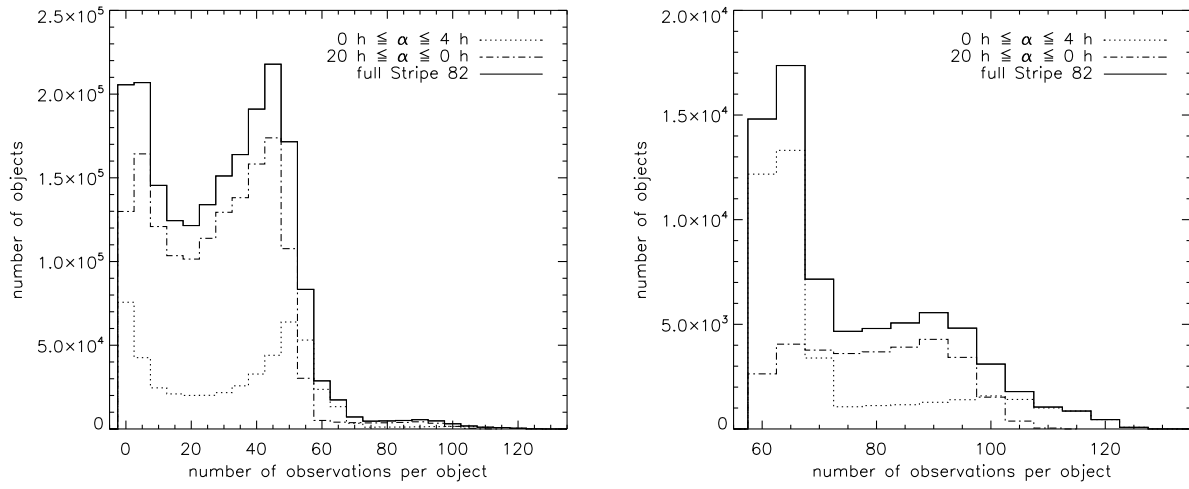


Fig. 3.— Left: Histogram of observations per object in the entire dataset spanning the years 1998 to 2007. The median number of observations is 30. Right: Histogram of observations per object for objects with at least 60 observations.

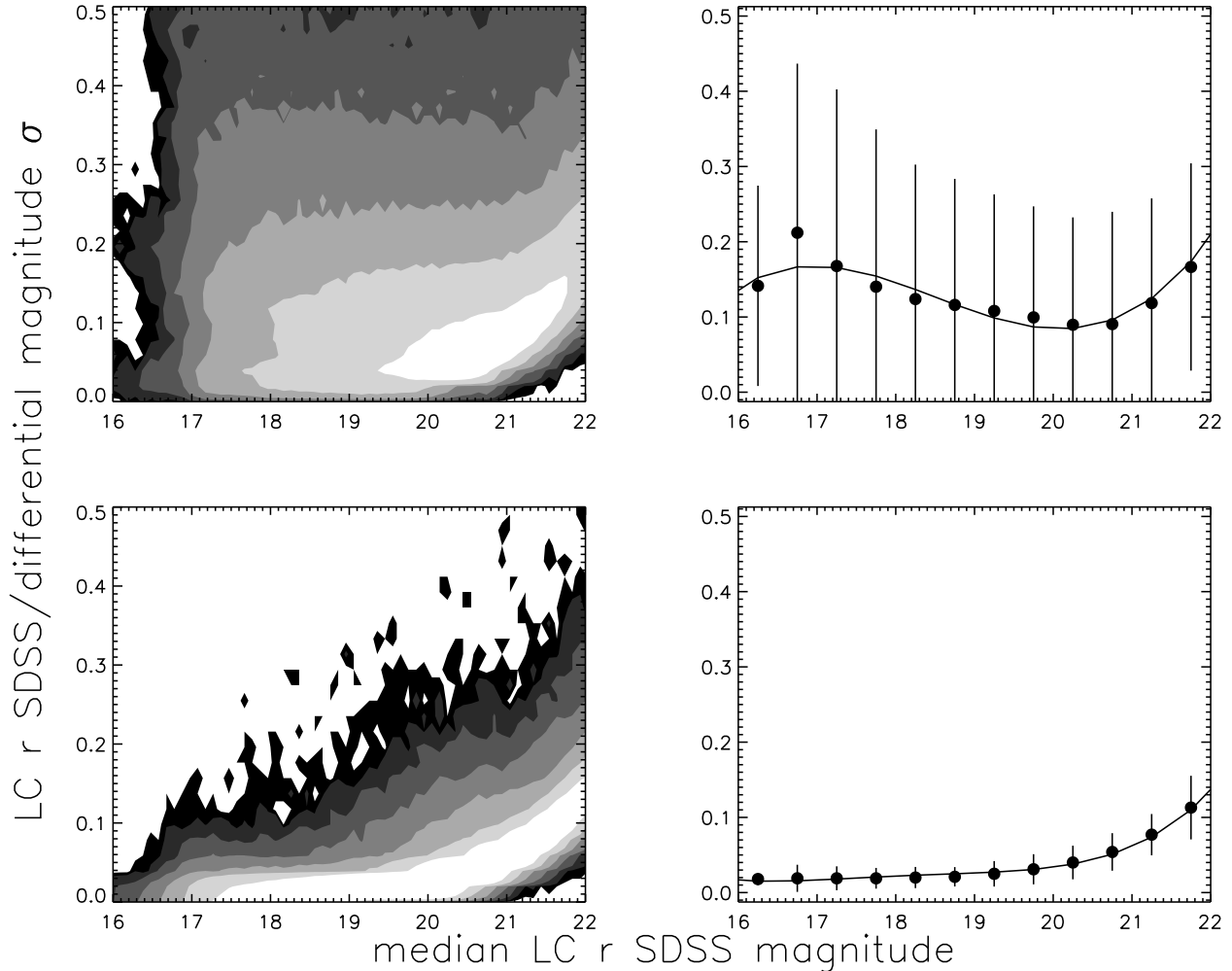


Fig. 4.— Top-left: SDSS r median light-curve magnitude vs. SDSS r light-curve standard deviation. Top-right: Median SDSS r light-curve standard deviation plotted against median SDSS r LC magnitude, binned in 0.5 magnitude bins, for $16.0 < r < 22.0$. Bottom-left: SDSS r median light-curve mag vs. differential r light-curve standard deviation. The scatter in the magnitude- σ relation is much reduced. Bottom-right: Median differential r light-curve standard deviation vs. median SDSS r LC magnitude, binned in 0.5 magnitude bins, for $16.0 < r < 22.0$. ‘Error-bars’ represent the rms scatter for each bin of the respective light-curve standard deviation distributions. The lines are fourth-degree polynomial fits. All density contours are in half-dex increments ranging from 1.0 to 3.0.

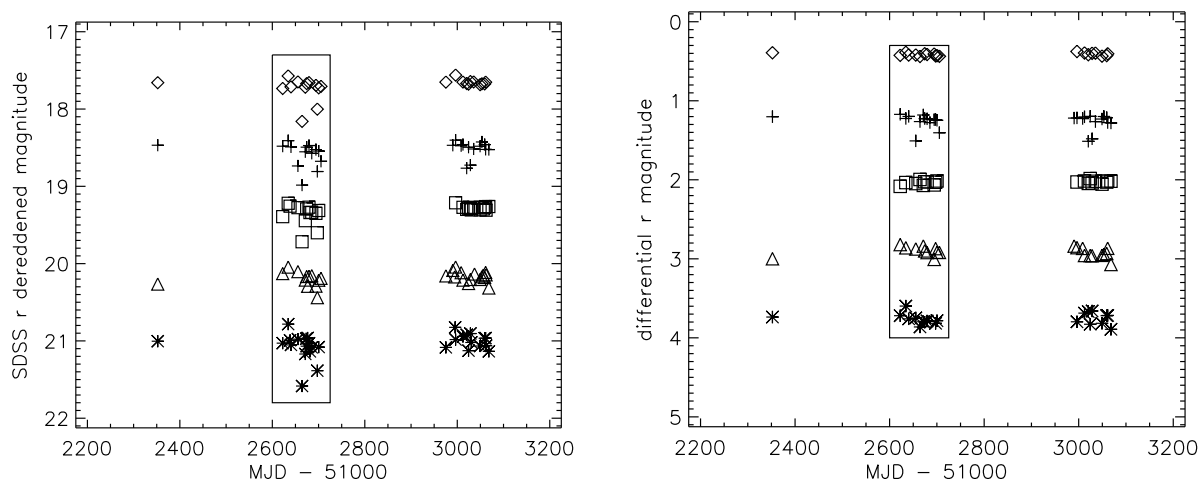


Fig. 5.— Left: SDSS r mag light-curve for an M3 dwarf eclipsing binary candidate (plus symbols) compared to its four closest neighbors (diamond, square, triangle, and asterisk symbols). Note that all five objects appear to have a light-curve dip on the same observation date (outlined by the box); this is an example of false variability caused by systematic effects from varying photometric conditions. Right: differential r light-curve after ensemble photometry carried out on the this field. Note that only the target object (plus symbols) appears to be variable: a possible eclipsing binary. The other objects no longer suffer from systematic effects that would have resulted in them being erroneously tagged as possible variables.

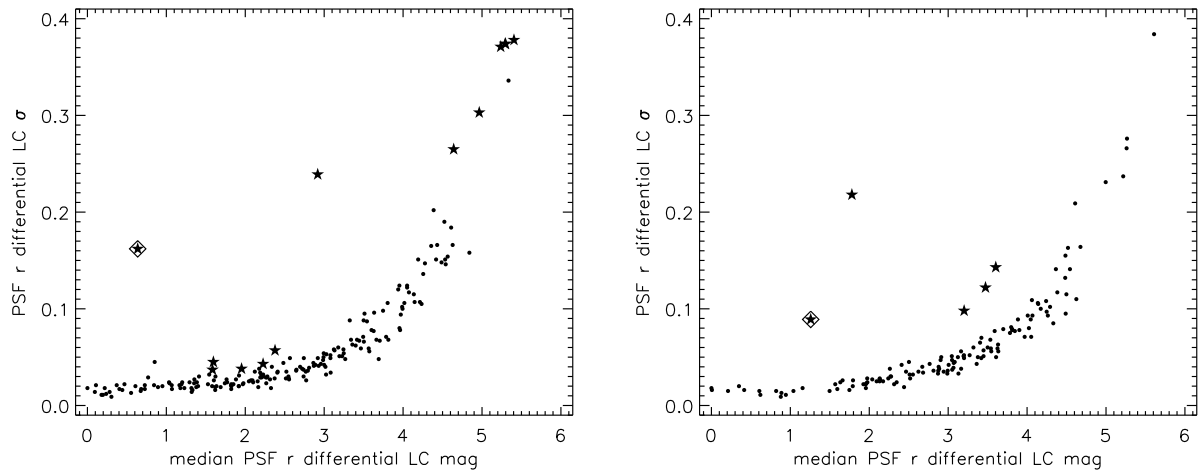


Fig. 6.— Examples of PSF r differential magnitude- σ trend plots generated by our ensemble photometry pipeline. These particular plots are for the comparison star ensemble fields of two objects eventually identified as periodic variables: MB875 (left panel) and MB32047 (right panel). Objects tagged by the ensemble photometry pipeline as *tentative variables* are shown as star symbols and the two periodic variables in the field are shown as stars inside the diamond symbols.

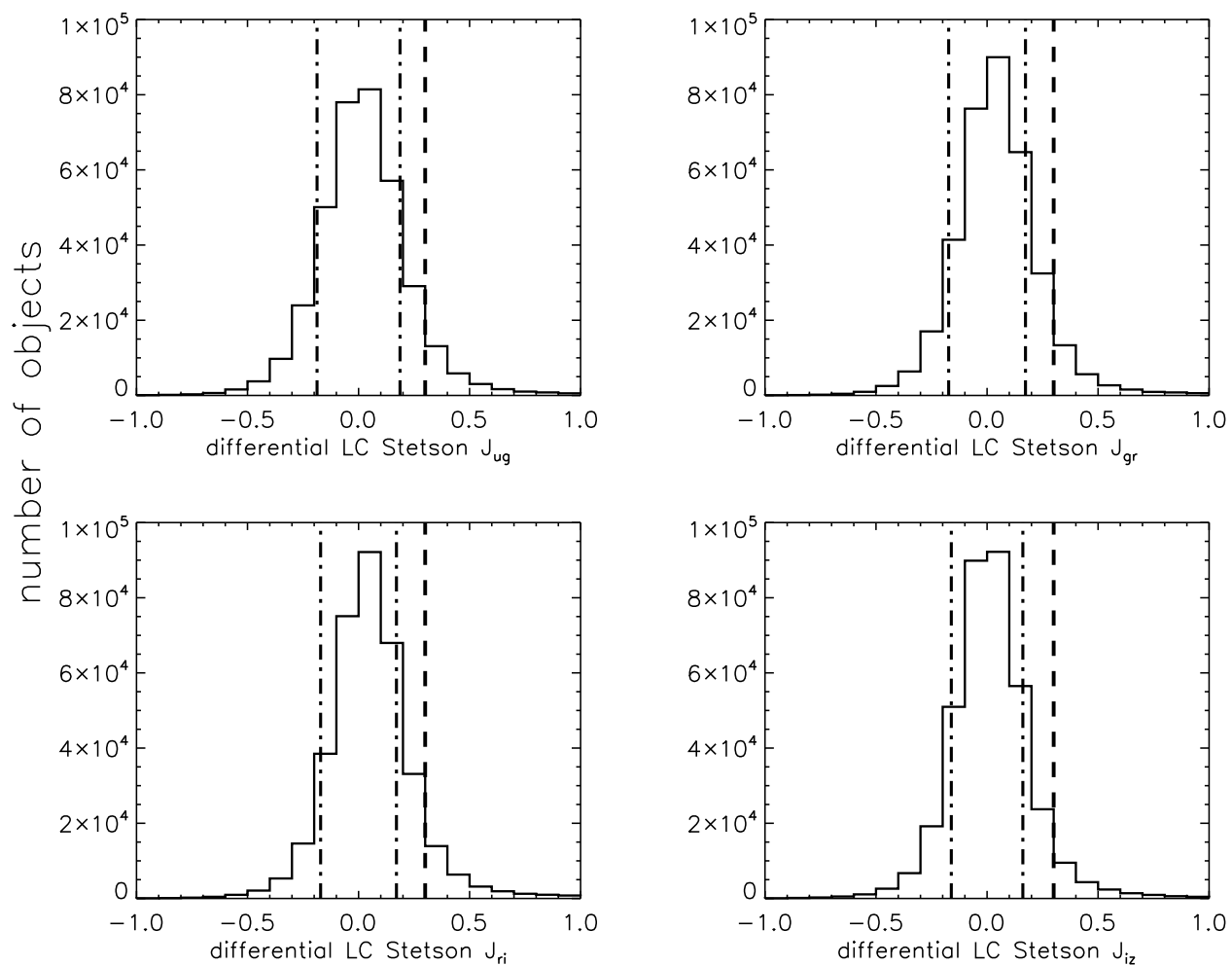


Fig. 7.— Stetson variability index histograms for all 365,086 objects with more than 10 detections in our RA 0 to 4 h light-curve catalog. The dot-dashed lines indicate the standard deviations of the distributions, while the dashed line indicates our threshold Stetson index value of 0.3.

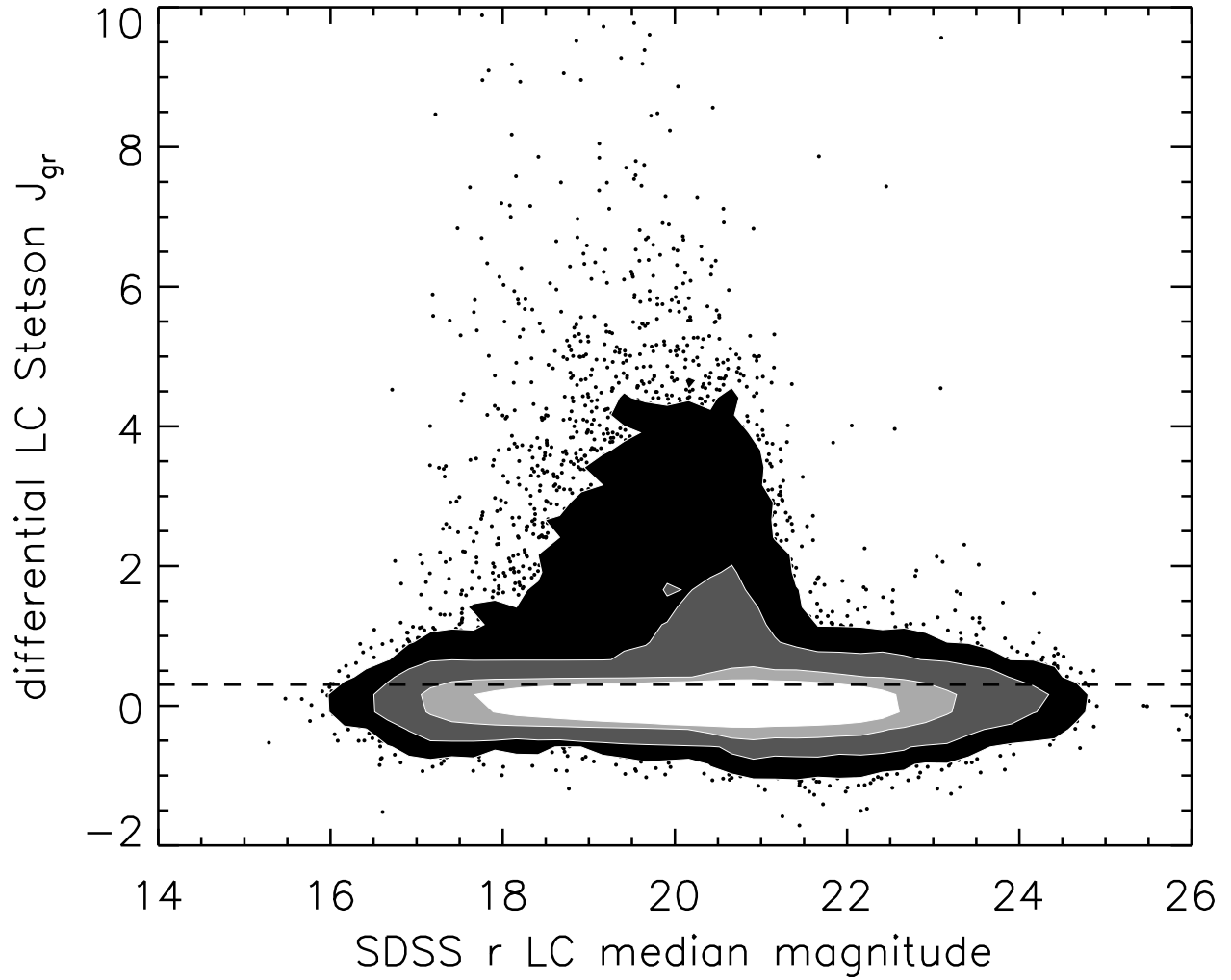


Fig. 8.— Stetson variability index J_{gr} vs. SDSS light-curve median r magnitude for all 365,086 objects with more than 10 detections in our RA 0 to 4 h light-curve catalog. The density contours are in dex increments ranging from 1.0 to 3.5, and the dashed line shows the minimum threshold value for variability detection, $J_{gr} = 0.3$.

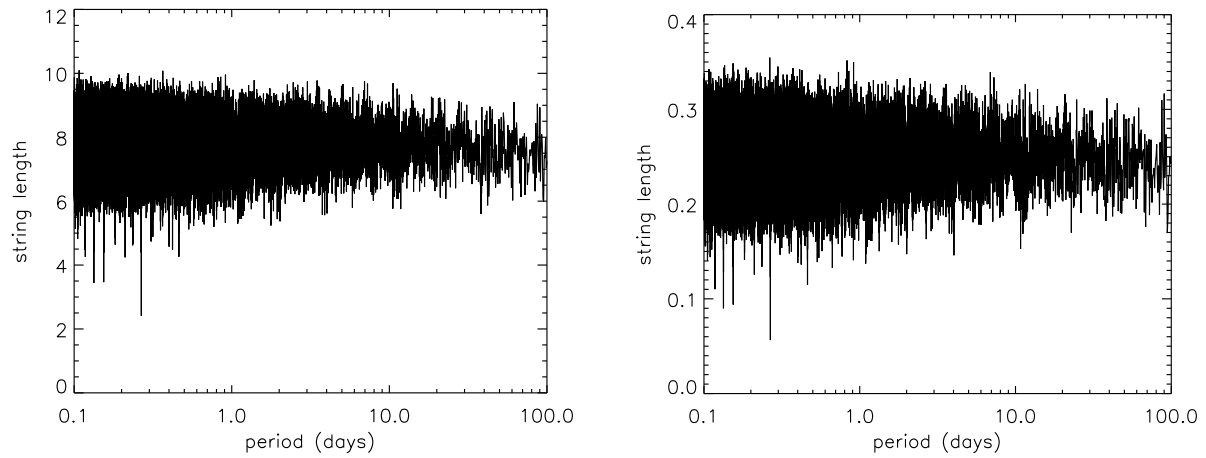


Fig. 9.— Left: differential g -band Dworetzky string length diagram for an eclipsing binary candidate (MB6467 in Figure 18). Right: differential g -band Stetson string length diagram for the same object. The smallest value of the string length in both cases indicates the most likely period, in this case; ~ 0.2668 days.

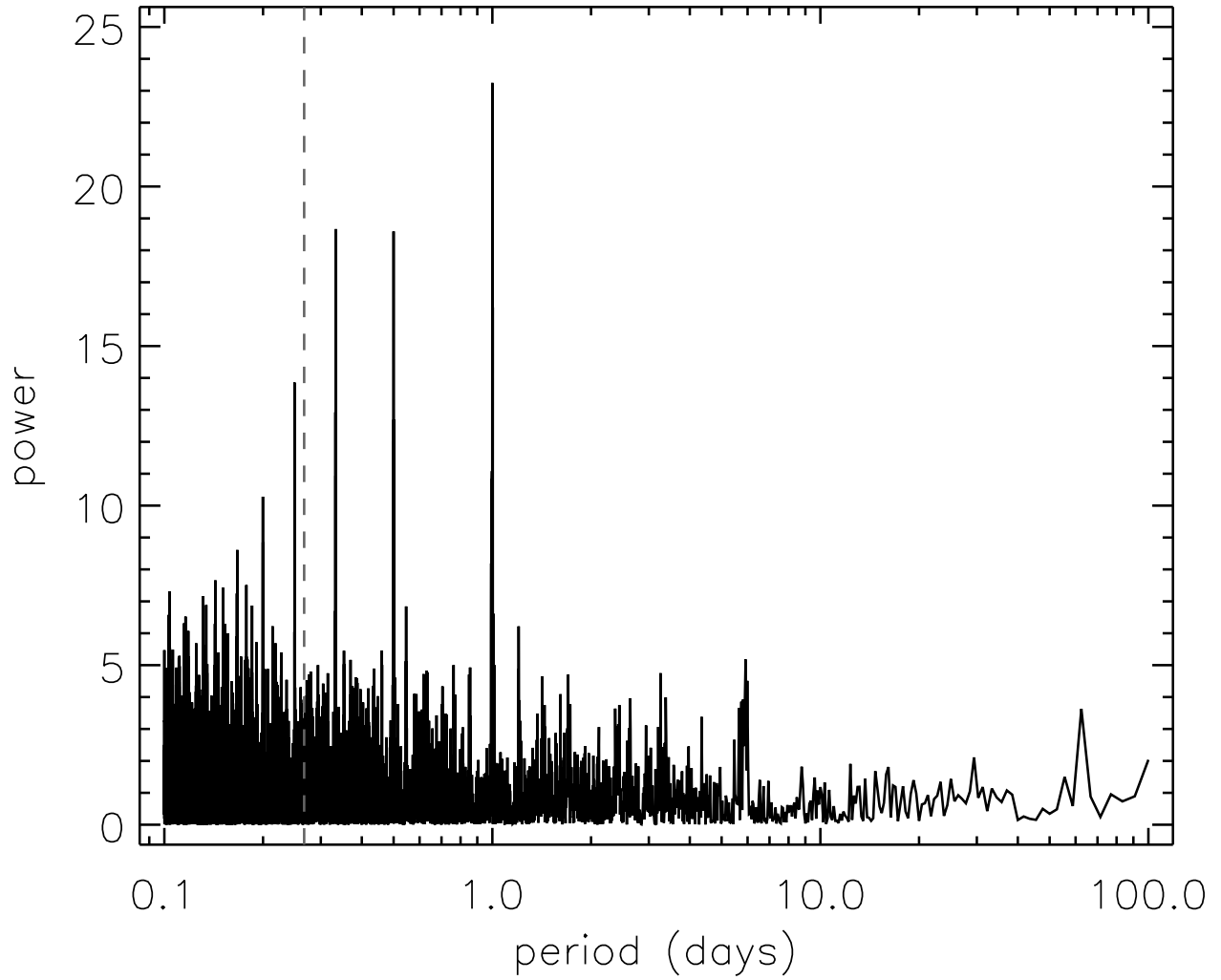


Fig. 10.— Lomb-Scargle periodogram for a typical spectral window function in the range 0.1 to 100.0 days. Note the strong peaks near 1, 7, and 30 days and their aliases. This window function was calculated using the g -band differential magnitude light-curve from the same object as in Figure 9. The period of this object is marked with the grey dashed line.

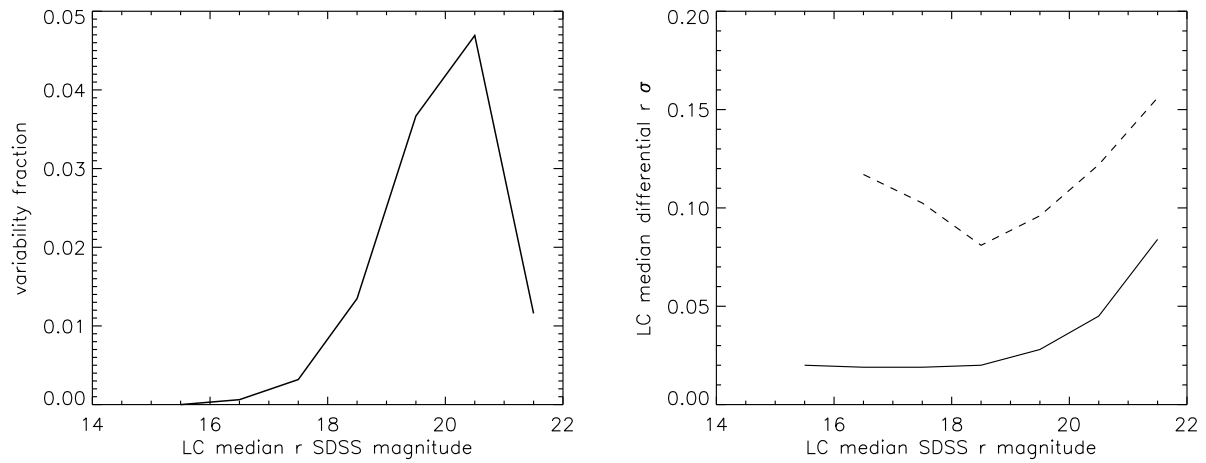


Fig. 11.— Left: The variability fraction as a function of r median SDSS light-curve magnitude for the $r < 22.0$ sample of 221,842 objects. Right: The median differential magnitude light-curve σ as a function of magnitude for objects marked nonvariable (solid line) and those tagged as probable variables (dashed line) for the $r < 22.0$ sample.

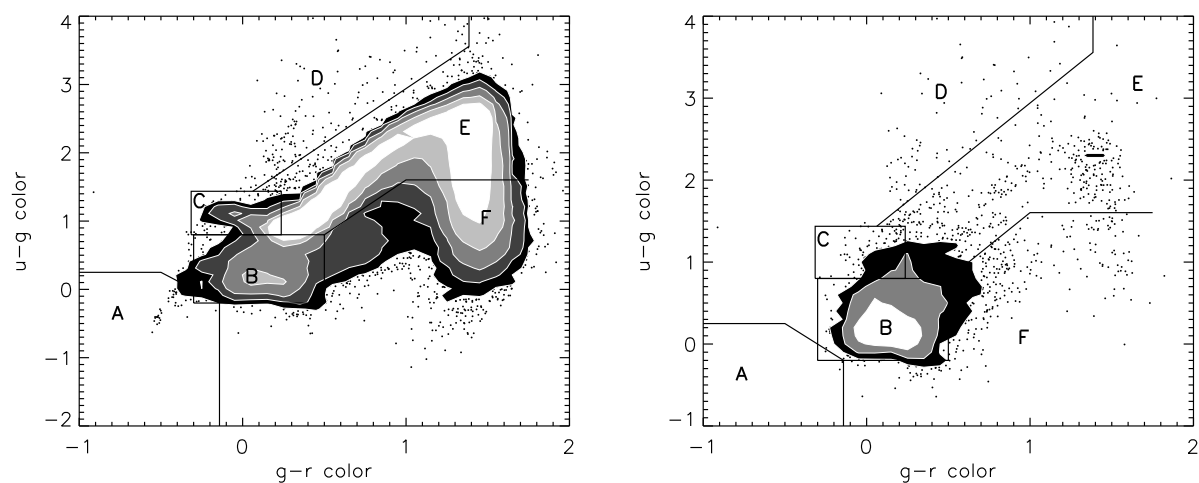


Fig. 12.— Left: SDSS $g-r/u-g$ color-color diagram for 221,842 point sources in our final light-curve catalog for RA 0 to 4 h. The density contours are in half-dex increments ranging from 1.0 to 3.0. Regions A–F indicate positions of various types of objects in color-color space: A. white dwarfs, B. low- z quasars, C. A/BHB stars (including RR Lyrae), D. hi- z quasars, E. main stellar locus, F. faint red objects (such as late M dwarfs and brown dwarfs). Right: The same diagram, this time only for 6,520 probable variable point sources identified by our pipeline. Note that the QSOs in region B dominate the numbers of probable variables detected.

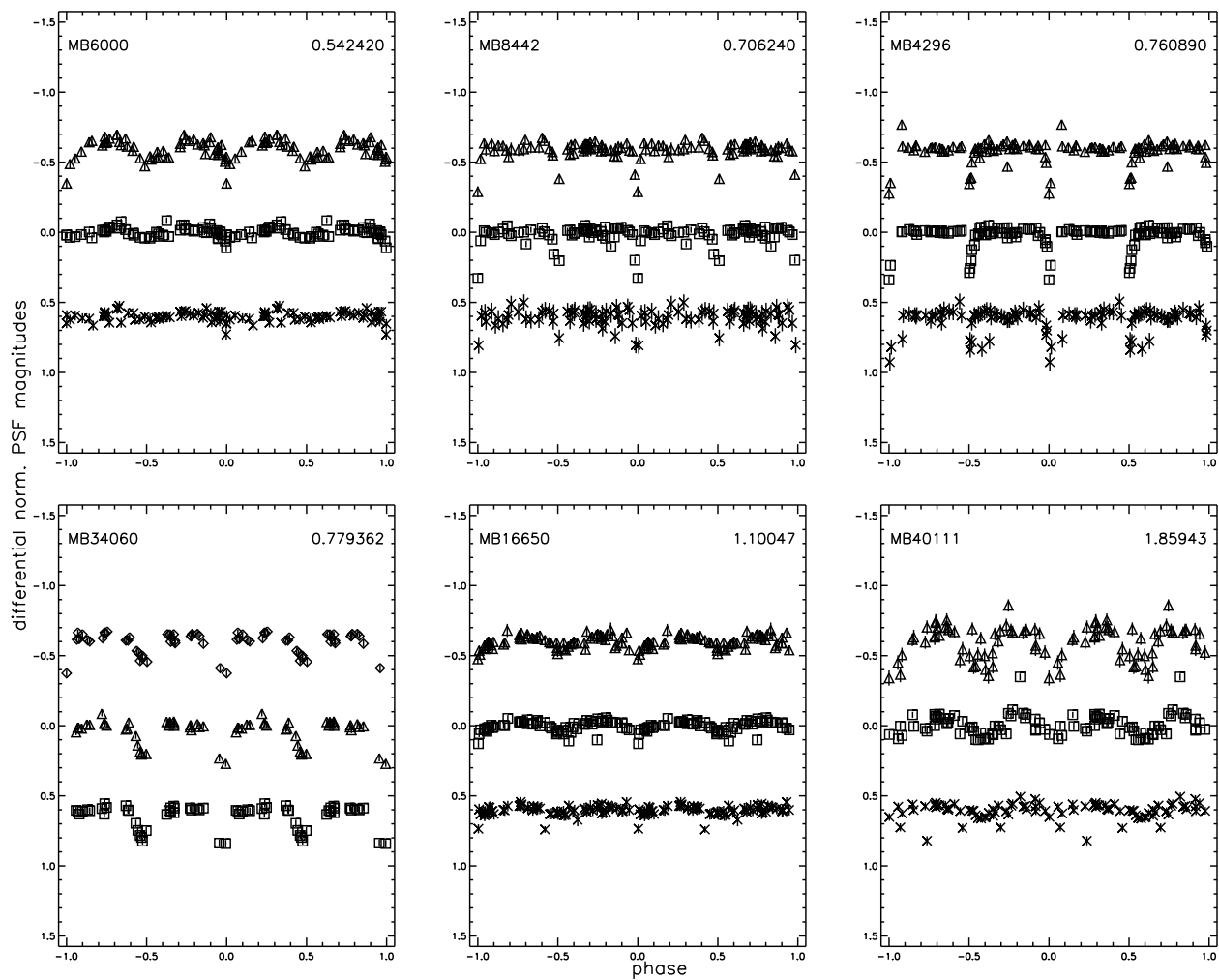


Fig. 13.— Phased differential magnitude light-curves for a sample of 6 objects with uncertain periods, in order of increasing period. The internal designation for an object and its best estimated period in days is shown in each panel. Diamond symbols are g light-curve points, triangle symbols are r light-curve points, box symbols are i light-curve points and cross symbols are z light-curve points. The light-curves are phased around the time of minimum light and repeated twice from phase -1 to +1 to clearly show variability.

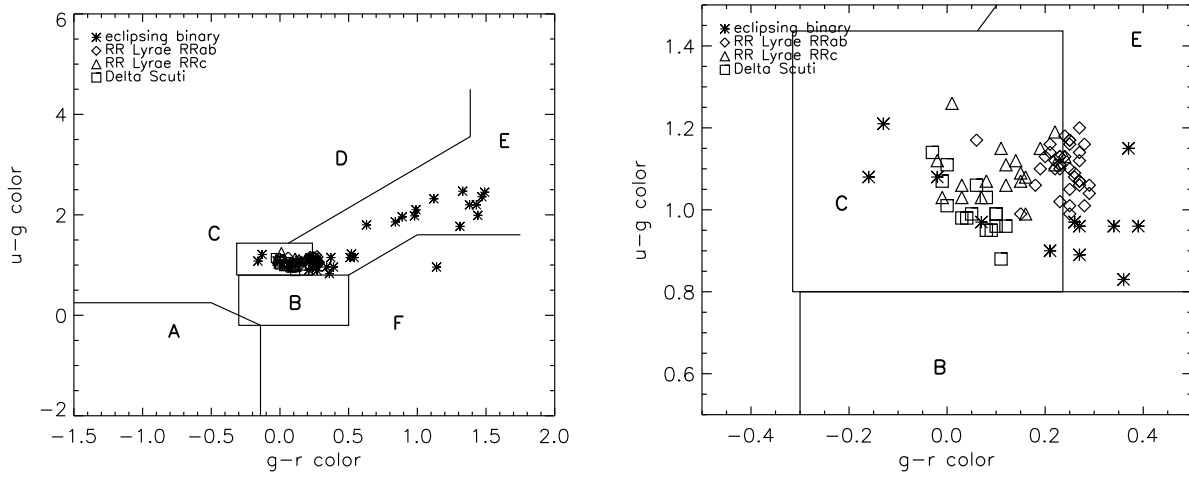


Fig. 14.— Left: Positions in $u - g/g - r$ color space of 101 periodic variables identified in this work. Regions A–F are the same as in Figure 12. Right: Same as in the left panel, but zoomed into region C.

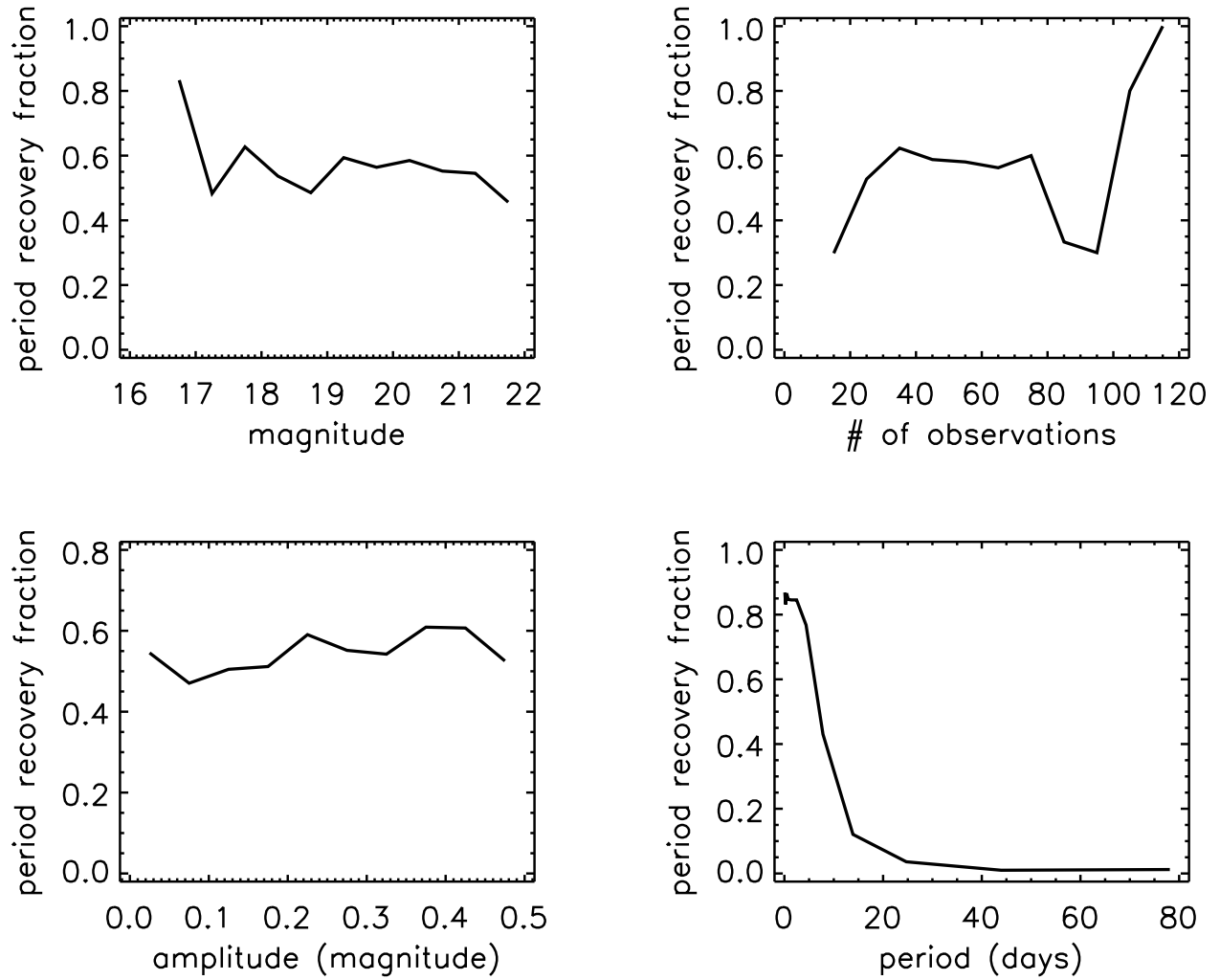


Fig. 15.— Top left: Period recovery fraction as a function of the median r magnitude of synthetic probable variables. Top right: Period recovery fraction as a function of the number of observations. Bottom left: Period recovery fraction as a function of the amplitude. Bottom right: Period recovery fraction as a function of the input period.

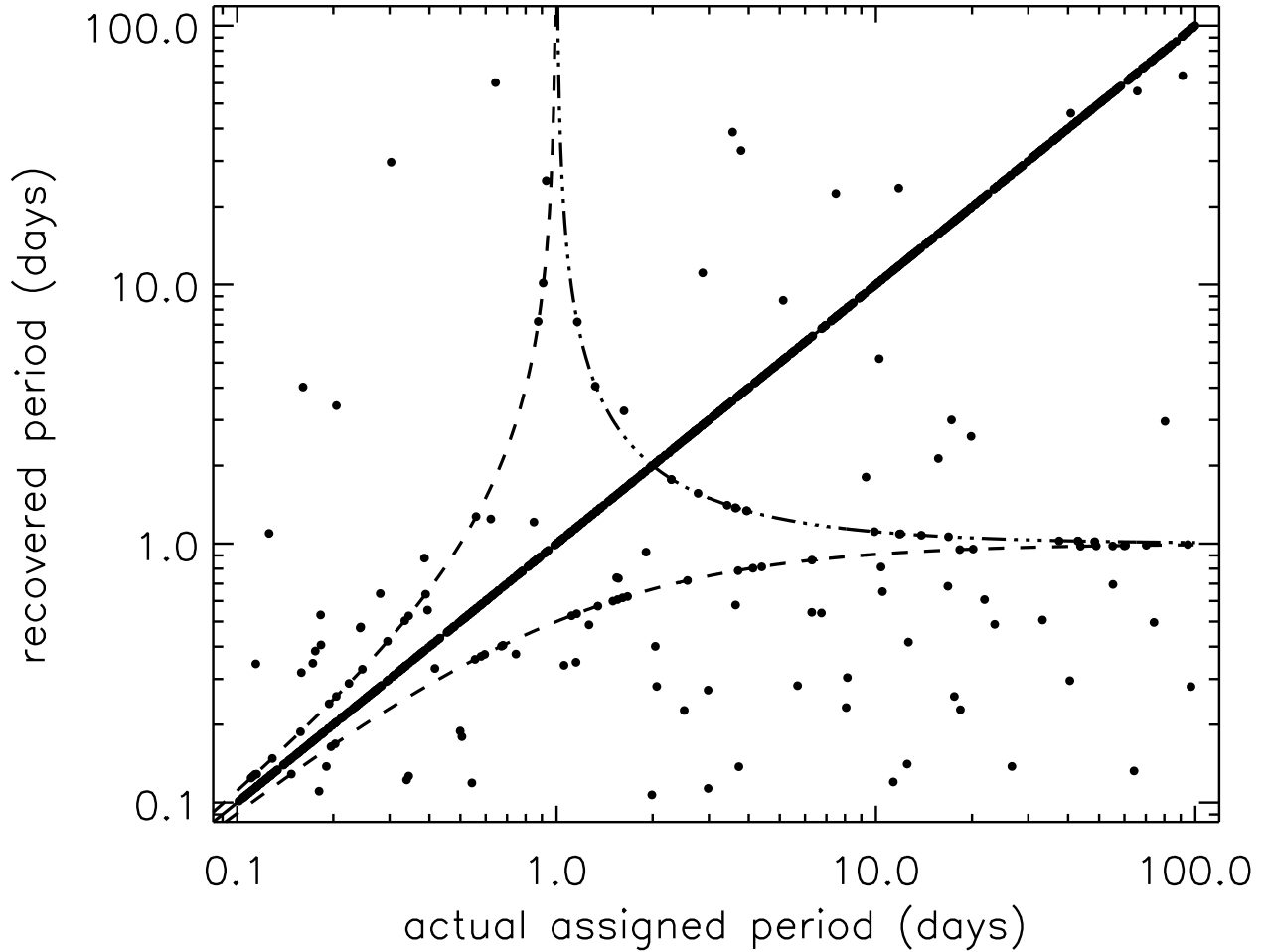


Fig. 16.— A comparison of assigned periods for artificial periodic variables and the period recovered by our pipeline. The solid line with unit slope indicates that the recovered and assigned periods are equal. The two dashed curves depict the relation $P_{recovered} = P_{assigned}/(1 \pm P_{assigned})$, while the dot-dashed curve depicts the relation $P_{recovered} = P_{assigned}/(P_{assigned} - 1)$. The solid circles are results of this experiment for each individual artificial periodic variable. Also see Figure 6 in Watkins et al. (2009).

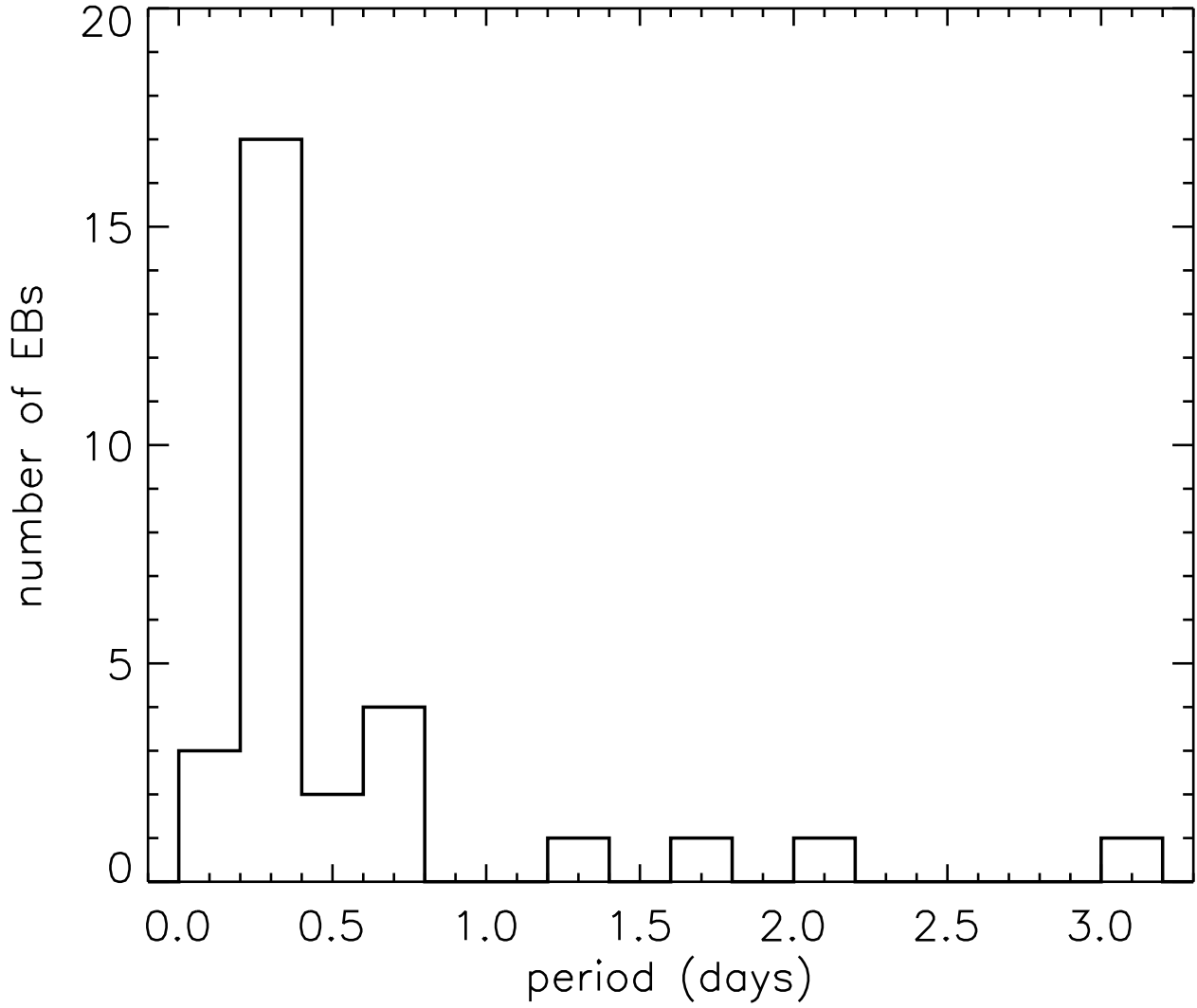


Fig. 17.— Period histogram for 30 eclipsing and ellipsoidal binary candidates from this dataset, using a bin width of 0.2 days. There is a distinct lack of objects with periods greater than 1.0 day.

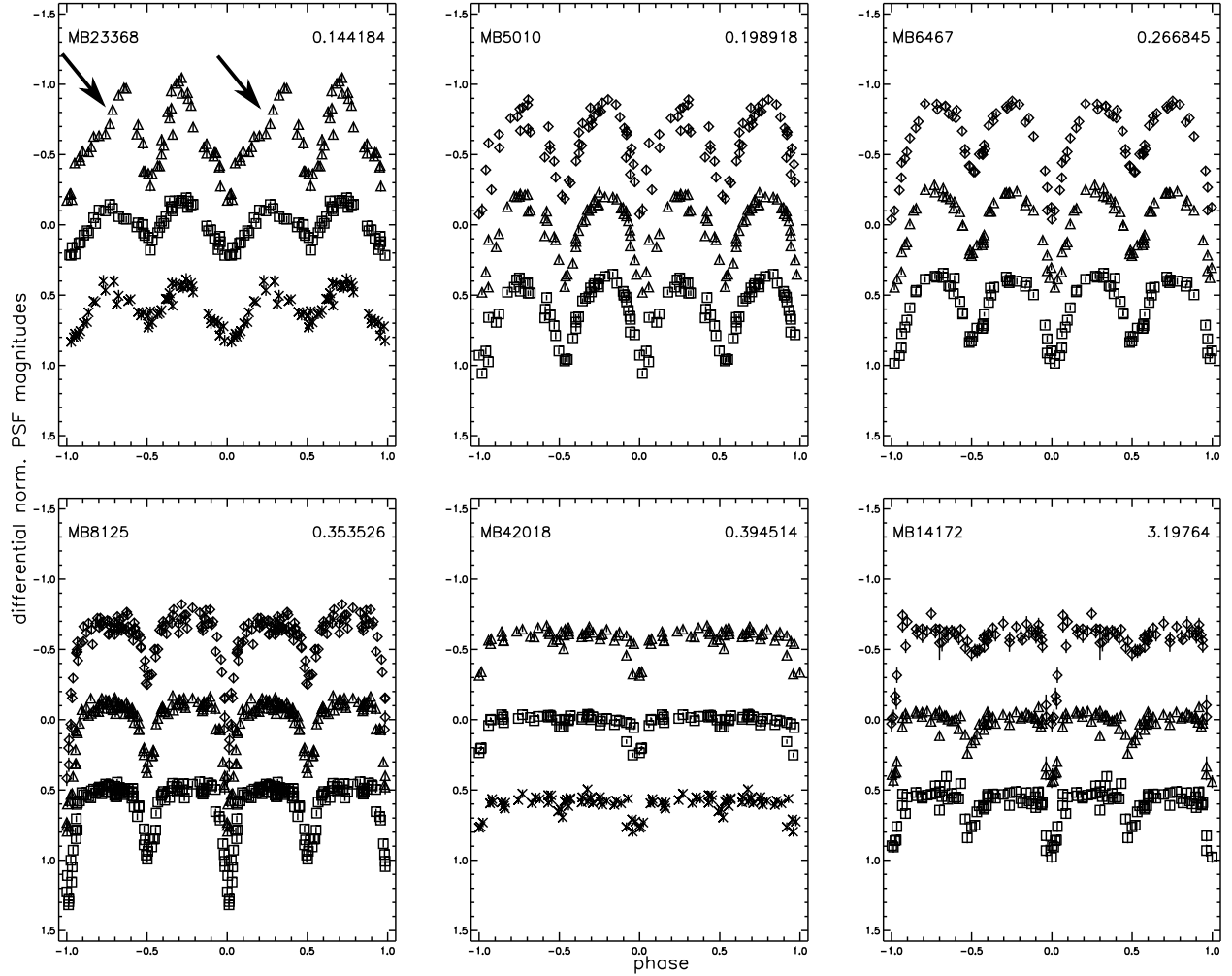


Fig. 18.— Phased differential magnitude light-curves for a sample of 6 eclipsing binary candidates identified by our pipeline, in order of increasing period. The internal designation for an object and its period in days is shown in each panel. Diamond symbols are g light-curve points, triangle symbols are r light-curve points, box symbols are i light-curve points and cross symbols are z light-curve points. The light-curves are phased around the time of minimum light and repeated twice from phase -1 to +1 to clearly show variability. The arrows point out the r -band out-of-eclipse variability observed for MB23368 mentioned in the text.

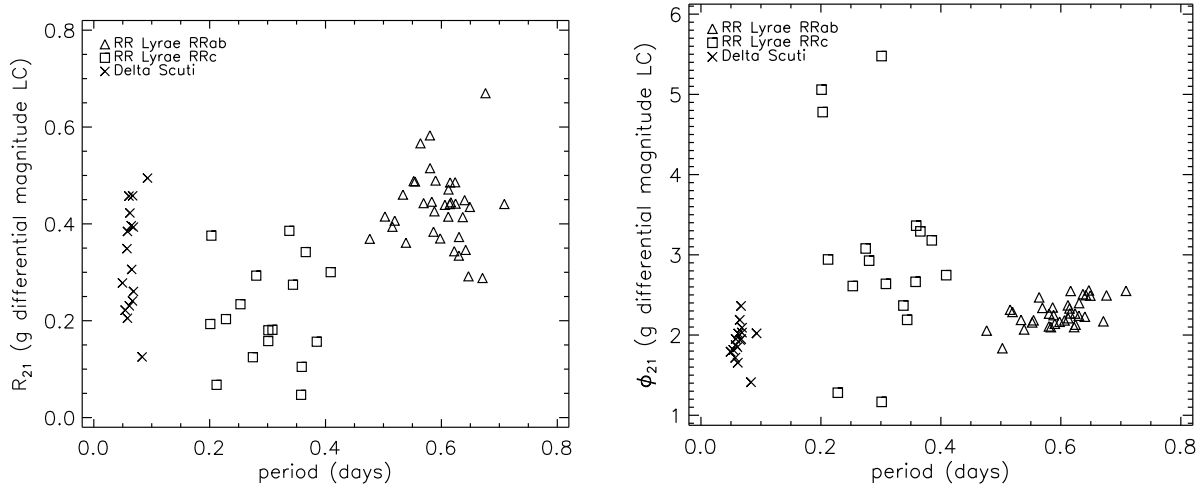


Fig. 19.— Left: Fourier parameter R_{21} calculated for g -band differential magnitude light-curves plotted against the period for RRab (triangles), RRC (boxes), and Delta Scuti variable candidates (crosses). The three sinusoidal variable types are easily distinguishable from each other. Right: Fourier parameter ϕ_{21} calculated for g -band differential magnitude light-curves plotted against the period for the same objects in the left panel.

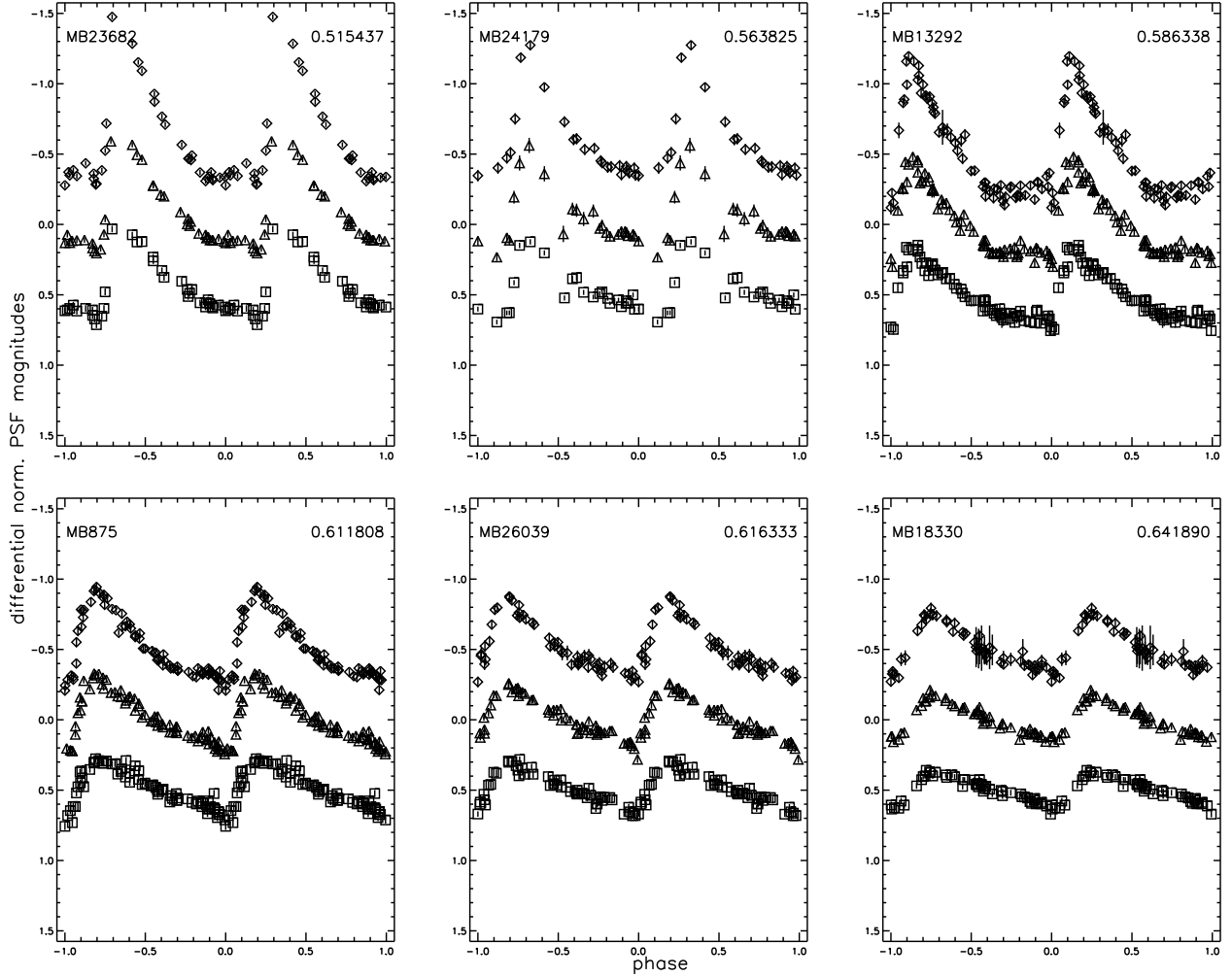


Fig. 20.— Phased *gri* differential magnitude light-curves for a sample of 6 RRab RR Lyrae candidates identified by our pipeline, in order of increasing period. The internal designation for an object and its period in days is shown in each panel. Diamond symbols are *g* light-curve points, triangle symbols are *r* light-curve points, and box symbols are *i* light-curve points. The light-curves are phased around the time of minimum light and repeated twice from phase -1 to +1 to clearly show variability.

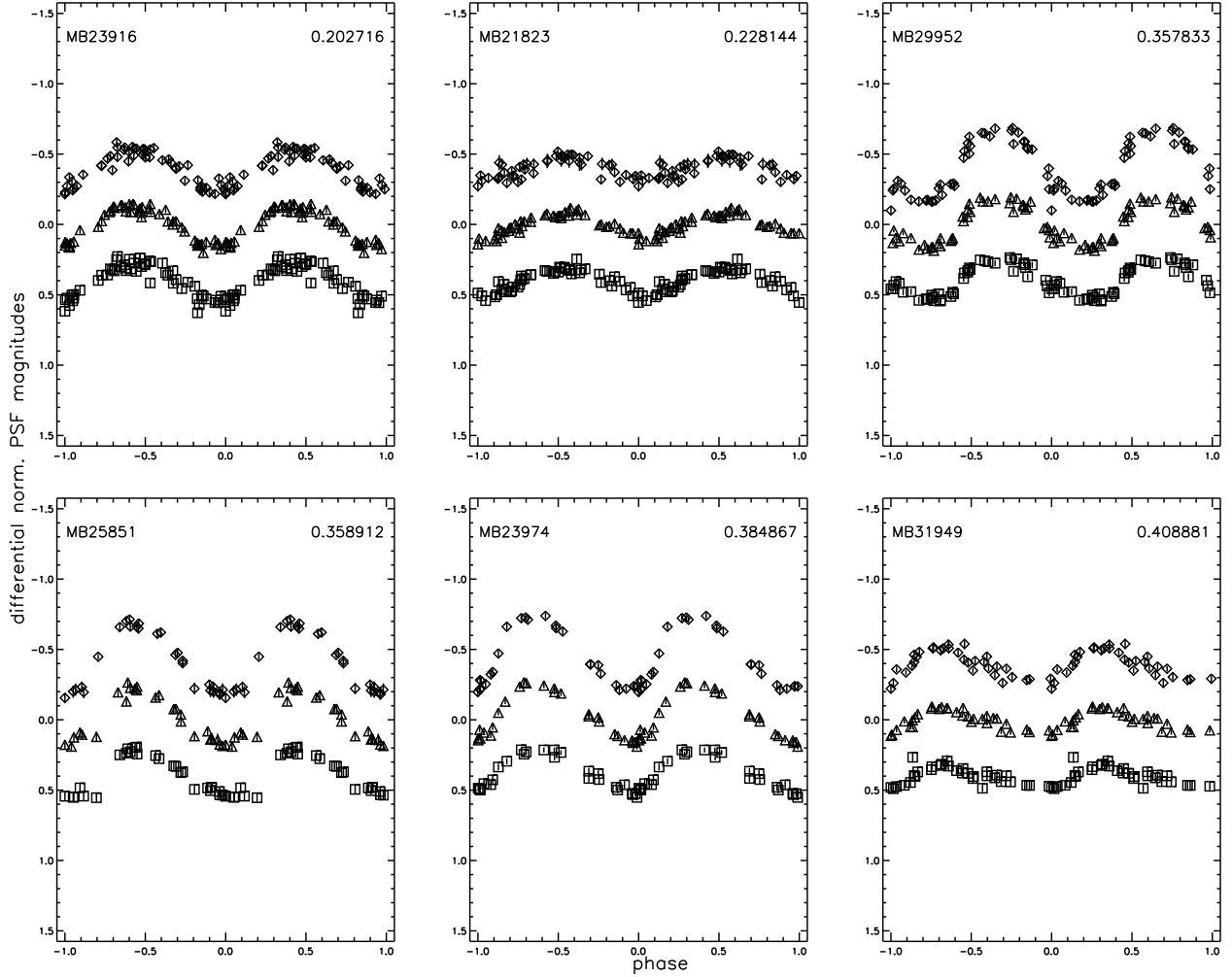


Fig. 21.— Phased *gri* differential magnitude light-curves for a sample of 6 RRc RR Lyrae candidates identified by our pipeline, in order of increasing period. The internal designation for an object and its period in days is shown in each panel. Diamond symbols are *g* light-curve points, triangle symbols are *r* light-curve points, and box symbols are *i* light-curve points. The light-curves are phased around the time of minimum light and repeated twice from phase -1 to +1 to clearly show variability.

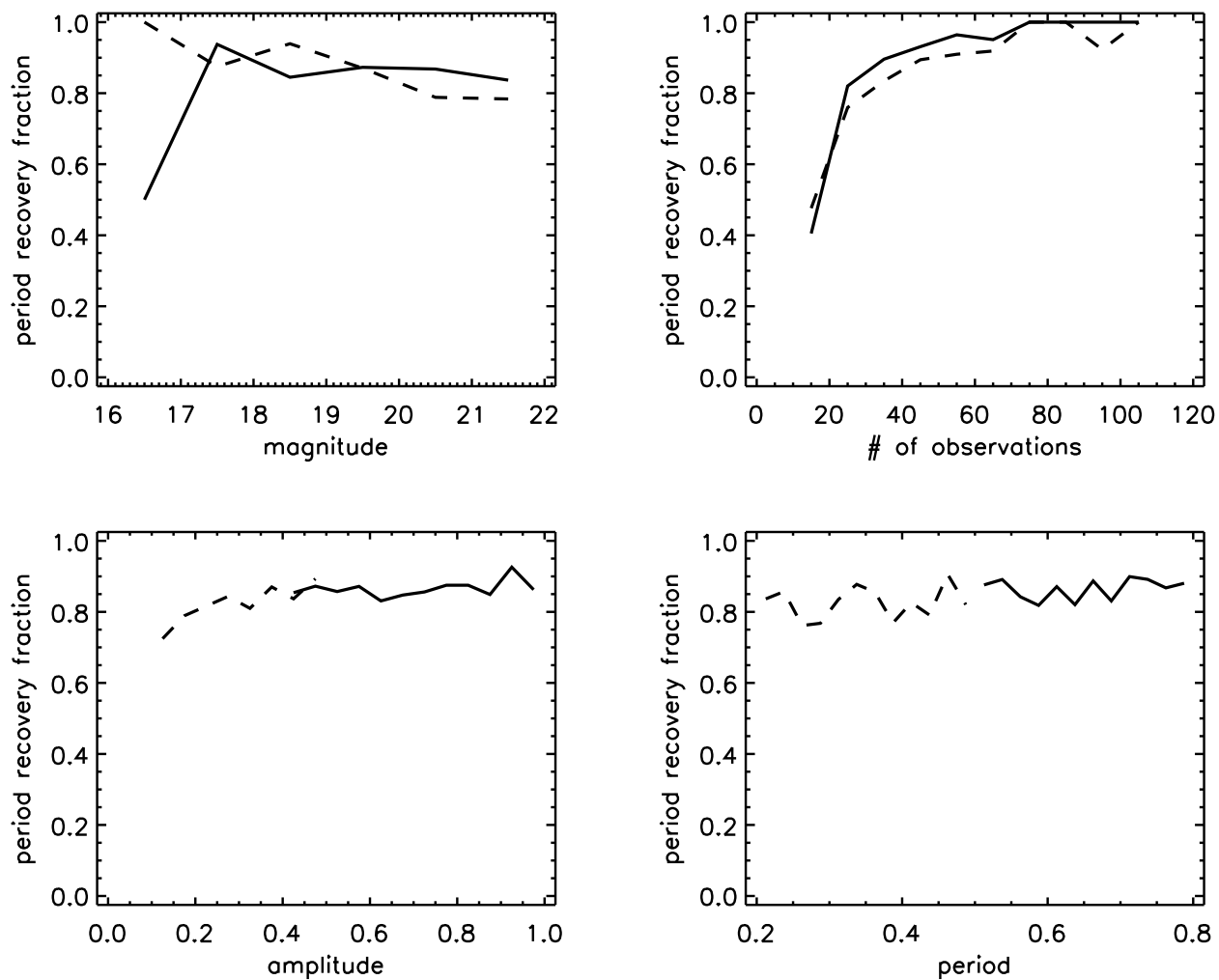


Fig. 22.— Top left: Period recovery fraction as a function of the median g magnitude of synthetic RRab and RRc probable variables. Top right: Period recovery fraction as a function of the number of observations. Bottom left: Period recovery fraction as a function of the amplitude. Bottom right: Period recovery fraction as a function of the input period. The solid lines are for the RRab variables, and the dashed lines are for the RRc variables.

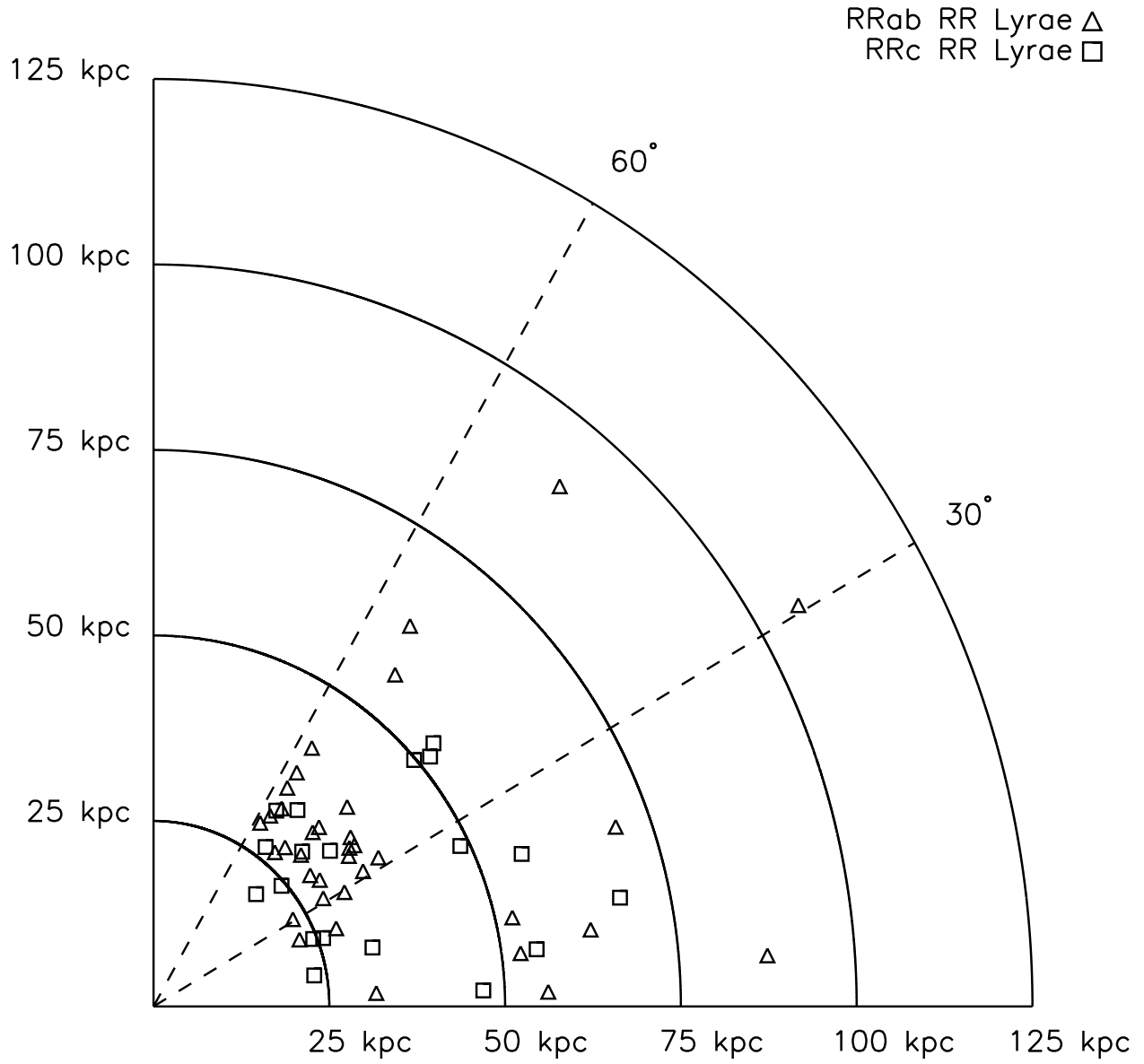


Fig. 23.— Distance vs. right ascension distribution of the 55 RR Lyrae in our dataset, which is restricted to a right ascension range of 0° to 60° , and a declination range of -1.27° to $+1.27^\circ$.

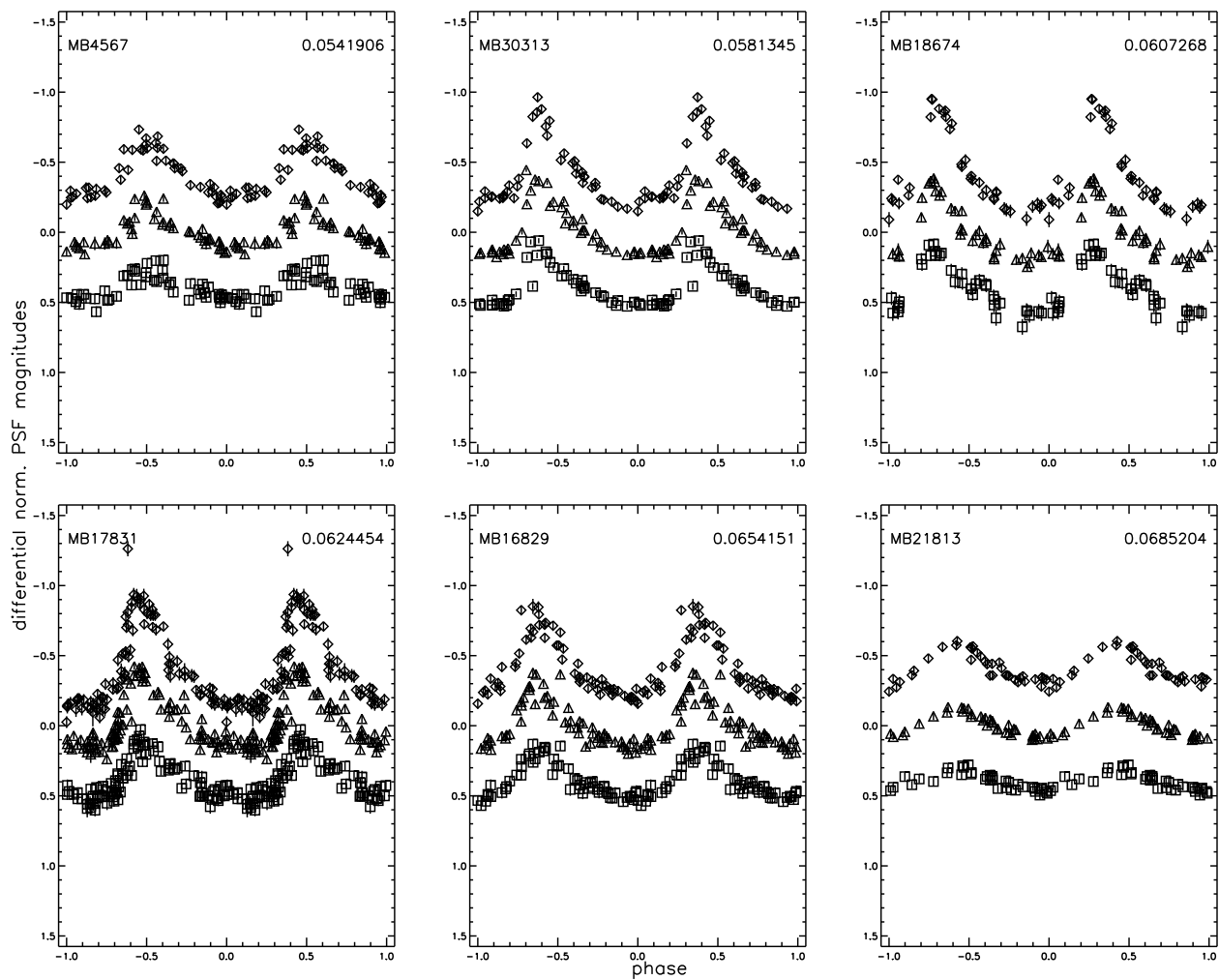


Fig. 24.— Phased *gri* differential magnitude light-curves for a sample of 6 Delta Scuti variable candidates identified by our pipeline, in order of increasing period. The internal designation for an object and its period in days is shown in each panel. Diamond symbols are *g* light-curve points, triangle symbols are *r* light-curve points, and box symbols are *i* light-curve points. The light-curves are phased around the time of minimum light and repeated twice from phase -1 to +1 to clearly show variability.

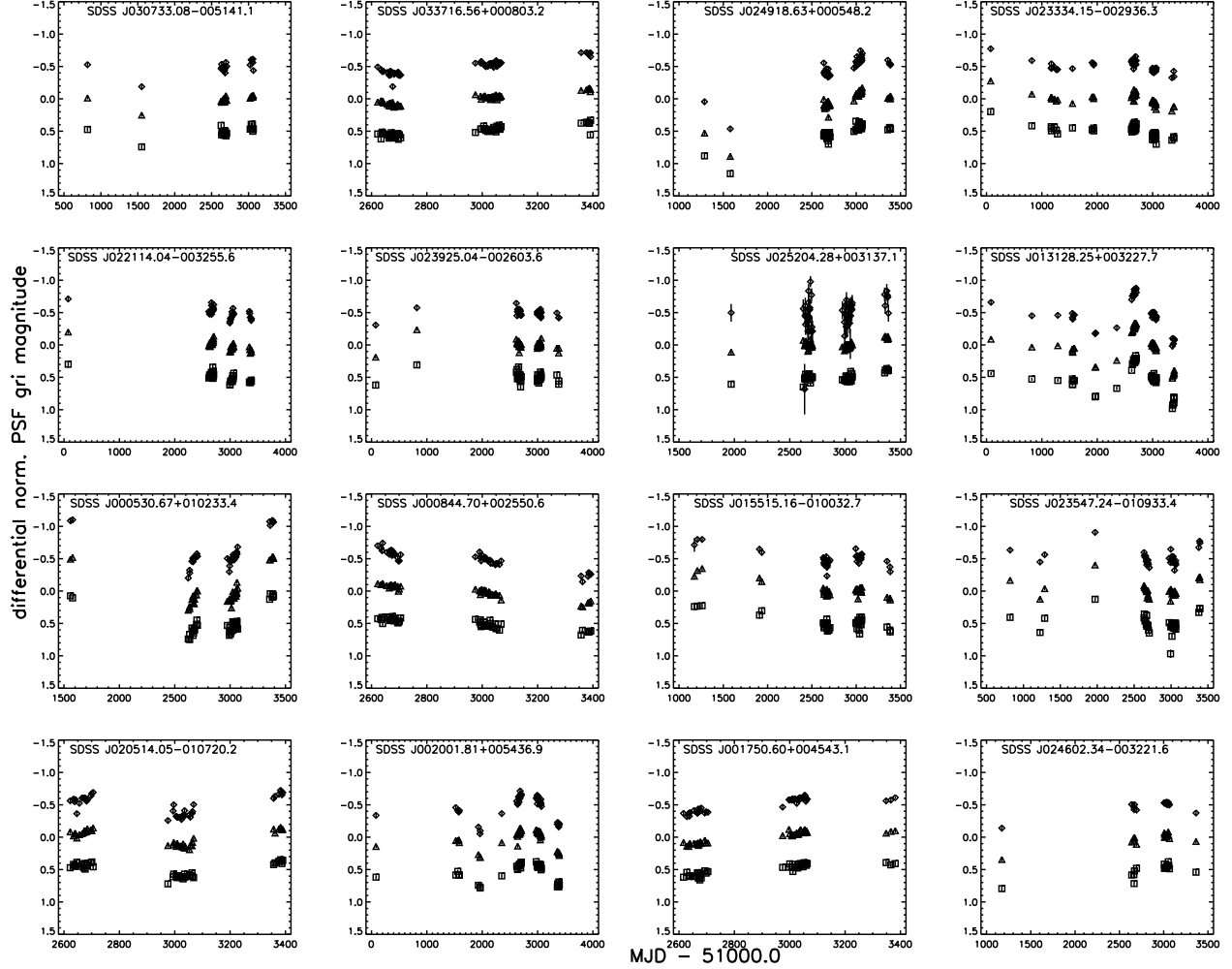


Fig. 25.— Differential magnitude *gri* light-curves for a random sample of 16 objects from the 2,704 quasars from the SDSS Quasar Catalog (Schneider et al. 2007) tagged as variables by our pipeline. Diamond symbols are *g* light-curve points, triangle symbols are *r* light-curve points, and box symbols are *i* light-curve points. The long term variability of these quasars is apparent over multi-year baselines.

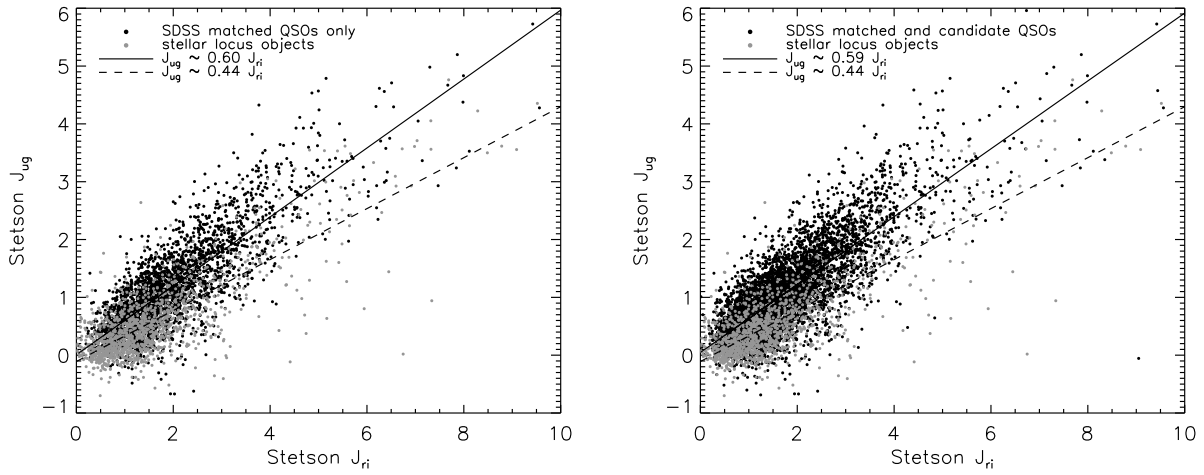


Fig. 26.— Left: Stetson variability index J_{ri} against J_{ug} for 2,704 variable QSOs (black circles) matched to the SDSS Quasar Catalog (Schneider et al. 2007) and 1,413 variable stellar locus objects (grey circles). The 2,403 new variable QSO candidates identified in this work are not included in this plot. Right: Stetson variability index J_{gr} against J_{ug} for all 6,520 probable variables tagged by our pipeline. The black circles are 2,704 variable QSOs matched to the SDSS Quasar Catalog plus 2,403 QSO candidates selected by color and variability. The grey circles are the remaining 1,413 variable stellar locus objects.

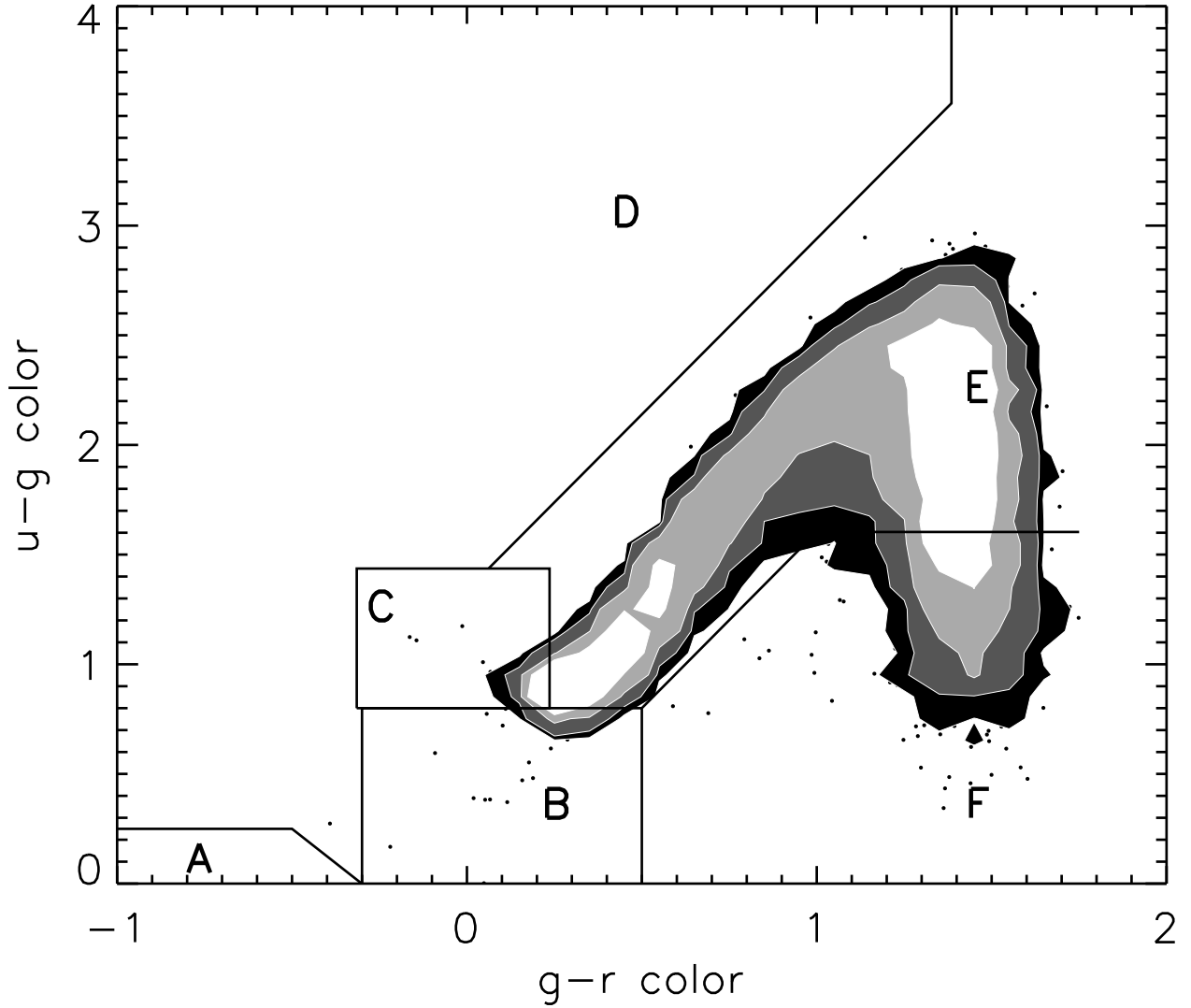


Fig. 27.— $g-r/u-g$ color-color diagram for 11,328 *probable nonvariable* point sources identified by our pipeline. Regions A–F are the same as in Figure 12. The density contours are in 0.5 dex increments from 0.5 to 2.0.